THEORETICAL AND EXPERIMENTAL STUDIES OF DROPLETS WETTING ON MICRO/NANO-FIBROUS MATERIALS AND THEIR APPLICATIONS IN OIL-WATER SEPARATION

A Thesis
Submitted to the Graduate Faculty
of the
North Dakota State University
of Agriculture and Applied Science

By

Meng Yu

In Partial Fulfillment of the Requirements
for the Degree of
MASTER OF SCIENCE

Major Department:
Mechanical Engineering

October 2013

Fargo, North Dakota

North Dakota State University
Graduate School

Title

Theoretical and experimental studies of droplets wetting on micro/nano-fibrous materials and their applications in oil-water separation

By

Meng Yu

The Supervisory Committee certifies that this ***disquisition*** complies with North Dakota State University's regulations and meets the accepted standards for the degree of

MASTER OF SCIENCE

SUPERVISORY COMMITTEE:

Dr. Xiangfa Wu
Chair

Dr. Dilpreet Bajwa

Dr. Xuefeng Chu

Dr. Yechun Wang

Approved:

11/5/2013	Dr. Alan R. Kallmeyer
Date	Department Chair

ABSTRACT

This research was aimed at the theoretical and experimental investigation of wetting behavior of immiscible droplets sitting on filaments and related applications in oil-water separation. This work consisted of three interrelated parts. Firstly, the engulfing behavior of two immiscible droplets sitting on a microfilament was studied theoretically; effects of the wetting properties and geometries of the droplet-on-filament system on the wetting morphology and capillary pressure were examined by detailed numerical simulations. Secondly, adhesion force and wetting area of a droplet bridge between two parallel plates were investigated via numerical simulation at varying contact angle and plate spacing. Finally, ultrathin continuous polymer nanofibers with very high hydrophobicity were produced by means of electrospinning technique. Experiments setup based on electrospun nanofiber membranes was demonstrated successfully for oil-water separation. The research results can be used to develop novel, low-cost, high-efficiency nanofibrous materials for oil-water separation and oil-spill sorption.

ACKNOWLEDGMENT

Firstly, I would like to thank my advisor Professor Xiangfa Wu for offering me the chance to work with him as a research assistant. With this opportunity, I gained a lot of knowledge and helps from him. Under the guidance of Dr. Wu, I quickly adjusted myself into my new graduate life at NDSU. Dr. Wu taught me not only knowledge, but also the way of how to conduct quality research. He even imparted me how to deal with difficulties in research and life. With Dr. Wu's supervision, enlightenments, and helps, I find that I am growing up quickly as a confident man. His charm on life, work ethic, and research enthusiasm has greatly inspired me.

I also give my great thanks to my supervisory committee members Professor Dilpreet Bajwa, Professor Xuefeng Chu and Professor Yechun Wang for their advice on my thesis research. With their great supports and constructive suggestions, I was able to accomplish my thesis work in a timely successful way. Special thanks to Dr. Yechun Wang for her generosity. Without her Lab tools, I cannot complete my experiment so successful.

I would also like to thank my team member Mr. Zhengping Zhou, who is the Ph.D. candidate in Dr. Wu's research group and has offered me huge valuable assistance in my experiment part. Without his assistance, I could not complete my experiments on oil-water separation so rapid.

Finally, I would like to thank the Department of Mechanical Engineering at North Dakota State University (NDSU) for offering me this precious chance to pursue my master's degree at NDSU.

Partial support of the research by the National Science Foundation, NDSU Development Foundation, and NDSU New Faculty Research Initiative Grant is gratefully appreciated. (www.ndsu.edu)

TABLE OF CONTENTS

LIST OF FIGURES

LIST OF ABBREVIATIONS

DMF ..... *N*, *N*-Dimethylformamide

IPDI ..... Isophorone diisocyanate

PAN ..... Polyacrylonitrile

PS ..... Polystyrene

SFEM ..... Surface evolver Finite Element Method

THF ..... Tetrahydrofuran

CHAPTER 1. INTRODUCTION

Nowadays, with the rapid development of modern industry and society, natural fossil resources (e.g., coals, petroleum, ore, etc.) are a very critical factor to a country's global competiveness and development potential. Among others, petroleum is one of the most important and commonly used resources to a country's economy. Due to the inevitable depletion of oil fields in land in the near future, people have gradually switched to explore petroleum of the earth stored in ocean bases such as the Mexican Gulf. So far, substantial technological progress in off-shore petroleum exploration has been made, and a bunch of off-shore exploring technologies and related facilities has been developed. From the perspective of energy use, technological advance can be a big solution to the development to society, because, to a great extent, it solves the upcoming problem of the deficiency in fossil fuels. Yet, in the viewpoint of environment, off-shore petroleum exploration may result in a huge challenge to the ocean ecosystem, which may also directly or indirectly impact the global ecosystem beyond the oceans. For instance, oil leakage from oil wells or explosion of underwater oil pipelines can be a disaster to the oceans and the human society as it has been evidenced in the aftermath of the oil leakage in the Gulf of Mexico, which has resulted in tremendous loss on both economy and ocean ecosystem .

Since a series of environmental problems has been caused by digging off-shore petroleum oils, protection techniques are under high demand in order to avoid any predictable disaster and to recover the ocean ecosystem if unpredictable accidents happen in the future. Among others, it is necessary for human being to develop and utilize innovative techniques to clean and recover seawater and ocean ecosystem quickly if polluted by oil leakage.

Rapidly increasing studies have been made on oil-water mixture in the past years. To mention a few, Behin (2008) obtained the residence time and distribution curves to examine the

influence of water level on oil-water separation, which described the flow behavior of crude oil and water in a pilot scale oil-water separator. In the perspective of materials science, Cheng (2009) designed novel polyethersulfone ultra-filtration membranes based on plurinic F127 for oil-water separation. This technique was initially studied by Li (2005) in developing novel UF membranes and Cheng (2009) refined the materials by grafting cellulose on polyacrylonitrile membranes. Apart from development of novel functional materials capable of oil-water separation or oil decomposition, people have also developed machines and tools for better performance on oil-water separation. For instance, Jin (Jin, 2013) developed a counter current gravity method for oil-water separation. In addition, people have been intensively working on complete separation of oil from water such as synthesis of novel superoleophobic materials, which can carry a better performance in oil collection than the traditional materials (Xue, 2013).

Although substantial research efforts have been made on studies of oil-water emulsion and its separation techniques, some relevant fundamental wetting principles and related experimental demonstration have not been completely elucidated. Thus, in this thesis work, we aimed at advancing the fundamental scientific understanding in oil-water separation and related development of novel materials and oil-water separation technique based on ultrathin polymer nanofibers produced by means of electrospinning technique. Specifically, Chapter 2 makes a briefly literature review on surface wetting and droplet wetting on fibrous materials. Chapter 3 discusses the wetting behavior of liquid bridge between two flat surfaces. Chapter 4 considers the wetting behavior of droplets of two immiscible liquids on fibers. Chapter 5 presents a novel oil-water separation technique based on electrospun nanofibers. Chapter 6 is the summary of the thesis work.

CHAPTER 2. LITERATURE REVIEW

Wetting and wicking of liquids on surface is universal and commonly observed in nature, life and engineering experiences, which has found extensive applications in environmental protection, oil cleaning, etc. Because of its important and significant role in many fields, the study of wetting and wicking phenomena has intrigued dedicated scientists and engineers all over the world to get involved. To date, substantial progress has been made to understand the wetting and wicking phenomena of droplet-on-filament systems. This literature review is to briefly introduce the fundamental knowledge and concepts of wetting and wicking of droplets on surfaces and the nowadays new understandings and findings of two droplets setting on monofilament.

2.1. Wetting, Dewetting, Contact Angle and Surface Tension

2.1.1. Introduction to Wetting and Dewetting

Wetting is the ability of liquid keeping contact with object surface; dewetting is the phenomenon describing the process of rupture and formation of liquid on the substrate, which may happen either between solid-liquid or between liquid-liquid. For an oil droplet sitting on water substrate, the spreading coefficient *S* describes whether the oil droplet dewets or spreads on the water substrate (Rosen, 2004):

$$S = \gamma_{vl} - \gamma_{vo} - \gamma_{ol} \tag{2.1}$$

where γ_{vl} describes the surface tension of vapor and water liquid substrate, γ_{vo} describes the surface tension between vapor and oil, and γ_{ol} is the interface tension of oil- water liquid.

If *S* is larger than zero, spreading occurs. In contrast, if *S* is small than zero, dewetting happens. In addition, the wetting ability varies in different liquids and substrates. Figure 2.1 illustrates the different wetting abilities (Wu and Dzenis, 2006):

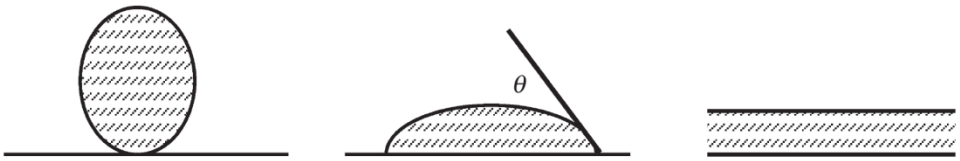

(*a*) (*b*) (*c*)

Figure 2.1. Different wetting abilities of liquid on solid substrate (Wu and Dzenis, 2006). (*a*): Entirely non-wetting situation, (*b*): Partially wetting case, and (c): Entirely wetting case

2.1.2. Liquid-Solid Contact Angle

Droplet wetting on solids is quite ubiquitous in nature. Two common cases are mostly studies, *i.e.*, droplet wetting on a surface and droplet wetting on filaments. Figure 2.2 illustrates the contact angle of a droplet wetting on a flat substrate.

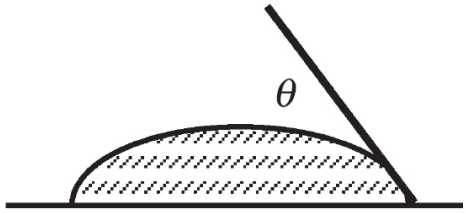

Figure 2.2. Contact angle of a droplet formed on a solid surface (Wu and Dzenis, 2006)

2.1.3. Liquid-Liquid Contact Angle

Similar to liquid-solid contact angle, two immiscible liquids can also form a contact angle, though the interaction between two liquids can be more complicated due to their inner pressures and interface tension. Figure 2.3 shows an optical image of a droplet of polyacrylonitrile (PAN) / *N*,*N*-dimethylformamide (DMF) solution and isophorone diisocyanate (IPDI) /DMF solution wetting on a microfiber fiber with the diameter around 10 μm. Due to the immiscible nature of PAN/DMF solution and IPDI/DMF solution, an interface between the two immiscible solutions can be clearly identified.

Figure 2.3. Interface between two immiscible droplets (with the assistance of Zhengping Zhou in Dr. Wu's research group at NDSU)

Here consider capillary phenomenon of a curved liquid surface as originally discussed by Butt (2006). The Young-Laplace equation is employed to describe the relationship between the pressure drop across a curved interface, ΔP, with the surface/interfacial tension γ and the local surface curvature κ

$$\Delta P = \gamma\kappa = \gamma\left\{\frac{1}{R_1}+\frac{1}{R_2}\right\} \tag{2.2}$$

where κ is the local curvature of surface, equals to $\left\{R_1^{-1}+R_2^{-1}\right\}$ (Diagram shows), R_1 and R_2 are the two principal radii of curvature of the curved liquid surface, and ΔP is called Laplace pressure. In the special cases, when $R_1 = R_2$, it is a sphere, then $\Delta P = 2\gamma/R$; when $R_2 = \infty$, it is a circular cylinder and $\Delta P = \gamma/R$. Two different types of molecules near the surface of a liquid are shown in Figure 2.4 (Booyabazooka, 2008).

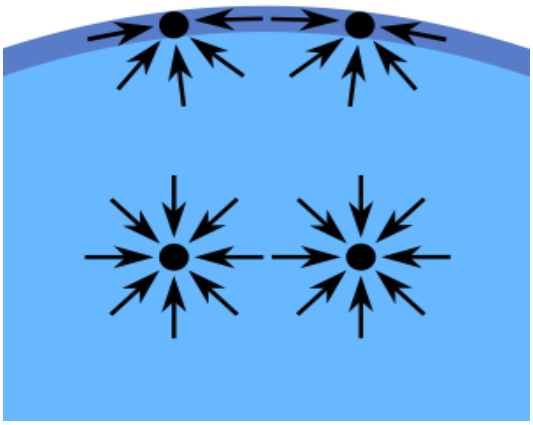

Figure 2.4. Molecules at the surface and inside liquid (Booyabazooka, 2008)

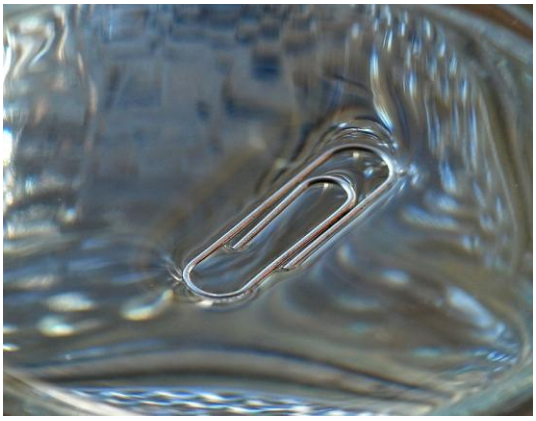

Figure 2.5. A light paper clip floats on liquid surface (Alvesgaspar, 2009)

Here are a couple examples to demonstrate how the surface tension works. Figure 2.5 shows a light paper clip floating on the liquid surface (Alvesgaspar, 2009). Figure 2.6 shows a dew droplet sitting on a leaf with a quite large contact angle because the leaf can be considered superhydrophobic material. It can be clearly observed that the leaf surface is quite unsmooth and covered with dense tiny needles, which provides the leaf a better resistance to water wetting. This phenomenon has been rationally explained by the Cassie-Baxter model (Apel, 2006).

Figure 2.6. A dew droplet sits on a grass leaf with a large contact angle (http://pictures.4ever.eu/nature/plants/drop-of-water-157854)

Interfacial tension is defined as the surface energy at the interface between two immiscible liquids, which can be explained using Girifalco-Good theory. Consider the liquid-solid interfacial adhesion, *i.e.*, the interfacial tension, which can be expressed as the geometric mean of the two surface free energies as

$$W = 2\left(\gamma_{sv}\gamma_{lv}\right)^{0.5} \tag{2.3}$$

According to Dupré's theory (Dupré, 1869) , the adhesion energy W can be expressed in terms of γ_{sv}, γ_{lv} and γ_{sl} as

$$W = \gamma_{sv} + \gamma_{lv} - \gamma_{sl} \tag{2.4}$$

Substitution of Eq. (2.3) into (2.4) leads to (Chaudhury, 1991)

$$\gamma_{sl} = \left\{\gamma_{sv}^{\ 0.5} + \gamma_{lv}^{\ 0.5}\right\}^2 \tag{2.5}$$

In the case of liquid-liquid interfacial tension, Girifalco-Good theory revised expression (2.4) by adding the interfacial term with a coefficient Φ as

$$\gamma_{sl} = \gamma_{sv} + \gamma_{lv} - 2\Phi\left(\gamma_{sv}\gamma_{lv}\right)^{0.5} \tag{2.6}$$

where $\Phi = \Phi_V.\Phi_A$ with Φ_V the molecular size and Φ_A the intermolecular force. Yet, it is needed to point out that such a revision does not noticeably improve the accuracy of γ_{sl}. Thus, Eq. (2.6) is adequate enough to estimate the interfacial tension of two immiscible liquids (Burkersroda, 1993).

In reality, very few cases exist such that two immiscible liquids carry the same surface tension under the same conditions, *i.e*, γ_{sl} cannot be equal to zero. However, in the limiting case that Eq. (2.6) is applied to water droplets, theoretically, γ_{sl} should be equal to zero by assuming that two water droplets are immiscible.

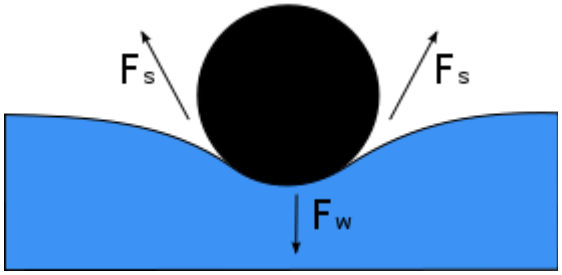

Figure 2.7. The schematic for interfacial tension (Hahn, 2009)

2.1.4. Wenzel and Cassie-Baxter Models

No ideally smooth surface (with zero surface roughness) exists in nature (Bormashenko, 2008). Thus, theoretical wetting models based on ideally smooth surfaces could not accurately predict the wetting behavior of liquids wetting on actual surfaces.

To take into account the effect of surface roughness on surface wetting, two wetting models have been formulated in the two limiting wetting cases, *i.e.*, Wenzel model (complete wetting) and Cassie-Baxter model (complete nonwetting). In Wenzel model, the apparent contact angle θ_1 on a rough surface is related to the surface roughness *r* and the ideal contact angle θ on the smooth surface (Marmur, 2003):

$$\cos\theta_1 = r\cos\theta \tag{2.7}$$

Wenzel's model assumes that the rough surface is completely wetted by the liquid at the equilibrium state, which is the limiting situation of real wetting surface.

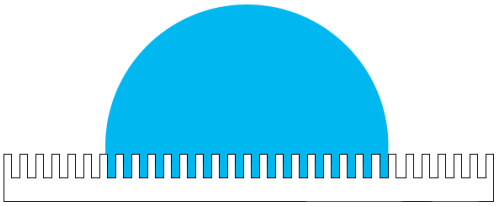

Figure 2.8. Schematic of Wenzal model (Okumura, 2008)

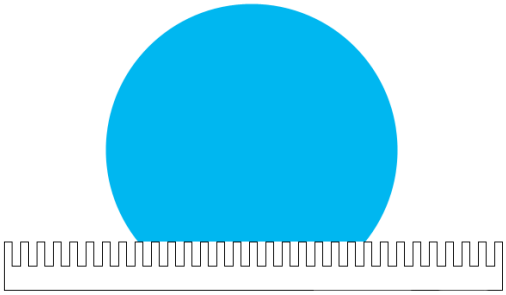

Figure 2.9. Schematic of Cassie-Baxter model (Okumura, 2008)

In contrast, Cassie-Baxter model is formulated with the assumption that the rough surface is completely non-wetted, which is the limiting situation for liquids wetting on rough, heterogeneous surfaces. According to Cassie's law, the apparent contact angle θ_2 is determined as (Marmur, 2003):

$$\cos\theta_2 = r_f f\cos\theta + f - 1 \tag{2.8}$$

where r_f is the roughness ratio of the wetting surface, f is the fraction of the solid surface wetted by liquid, and θ is the contact angle on an ideally smooth surface. Apparently, when f is equal to 1 and r_f is equal to r, Cassie-Baxter model is transferred to Wenzel model. The above relation only considers one material wetted by liquid. When the rough surface is made up with several

materials, the fraction of surface roughness should be the sum of f_i of several material components. Herein, f_i stands for the fraction of each material. By using relation (2.8), Cassie-Baxter model for multi-material surface can be obtained (Whyman, et al, 2008):

$$r\cos\theta = \sum f_j(\gamma_{j,SV} - \gamma_{j,SL}) \tag{2.9}$$

Consider a special case that a liquid drop is placed on a substrate with small air pockets trapped underneath, which can be treated as a two-component system such that

$$\gamma\cos\theta_2 = f_1\left(\gamma_{1,sv} - \gamma_{1,sl}\right) + \left(f_1 - 1\right)\gamma \tag{2.10}$$

where γ is the surface tension between the liquid and vapor, $\gamma_{1,sv}$ is the vapor-solid surface tension of each component, and $\gamma_{1,sl}$ is the liquid-solid surface tension of each component.

2.2. Liquid Bridge Phenomenon

2.2.1. Description

When a tiny droplet is trapped between two solid surfaces, a liquid bridge forms. The phenomenon of liquid bridge is commonly observed in daily life. It is meaningful when the system is considered in the microstructural level. In order to gain a direct view on this phenomenon, two macrocosmic objects can be used to manipulate a microcosmic structure if there is no apparent effect on the target, in other words, the physical properties are almost the same (Lambert, 2006). As aforementioned, although the phenomenon is commonly observed in nature, it contains rich physical meanings such as the capillary adhesion by a droplet between two solid surfaces and the capillary torque exerted by an asymmetric droplet between two misaligned filaments. In addition, it is important to determine the critical force leading to the breakage of a liquid bridge, i.e., the external force is needed to destroy the liquid bridge system (Swain, 2000). This critical force is termed as adhesion force, expressed as:

$$F = 2\pi r\gamma \sin\theta - \Delta p * \pi r^2 \tag{2.11}$$

Once the condition is varied such as the two solid surfaces are switched from the same materials to two dissimilar materials, the contact angles, wetting characteristics as well as the wetting length will change correspondingly. If two flat solid surfaces bridged by a droplet are replaced by one curved surface (*e.g.*, semispherical surface) and a flat surface bridged by a droplet, the situation will also be different.

2.2.2. Current Research

Due to the importance of liquid bridge in the fundamental understanding of capillary phenomenon, substantial attention has been paid on this topic (Gao, 2011). As a simple approximation in the literature, it is commonly assumed that the boundary curve of liquid bridge is a part of the sphere, which implies that the profile of the liquid bridge carries a given radius once the liquid volume is given. However, such an *ad hoc* approximation does not meet the experimental observations. An improved theoretical description would assume the profile of the droplet bridge is unknown. In Chapter 3, an improved governing equation of liquid bridge is established; a numerical method based on surface finite element method (SFEM) is employed to explore the wetting behavior of a liquid bridge system.

2.3. Droplet Wetting on Fibers

2.3.1. Background and Progress

In the simplest case of a droplet wetting axisymmetrically on a filament as shown in Fig. 4.1(*a*) . Carroll first obtained the explicit solution of barrel-shaped droplet morphology (Carroll, 1976). Several follow-up refinements have been made to consider the droplet roll-up and spreading behavior and enhance the accuracy in extracting the contact angle from wetting experiments based on various droplet-on-filament systems (Carroll, 1986; Wagner, 1990; Song

etal., 1998; Wu and Dzenis, 2006). In addition, by extending Carroll's work (Carroll, 1976), Wu et al. (Wu et al., 2010) and Liu et al. (Liu, 2013) considered the effect of fiber deformation on the wetting behavior of a droplet wetting on a soft micro/nanofiber. Du et al. (2010) examined the profile of a droplet at the tip of a filament. Brochard (1986) and Neimark (Neimark et al., 1999) formulated the kinetic and thermodynamic theories on the stability and spreading behavior of liquid droplets and films on filaments involving the disjoining pressure. Besides, Chen et al. (2001) considered the wicking kinetics of a droplet wetting on a microfiber yarn. Lorenceau and Quéré (2004) investigated the spreading of droplets on a tapered filament and concluded that the droplets move toward the region of lower curvature and the driving force is the gradient of Laplace pressure. Lorenceau et al. (2004) also studied the capture of droplets impacting on a horizontal fiber and a kinetic relation was gained. When taking into account the effect of gravity, Huang et al. (2009), Gilet et al. (2009, 2010), and Duprat et al. (1999) identified the conditions for the stability and sliding of droplets on inclined and vertically-positioned fibers which were validated by their experiments. Furthermore, a droplet sitting on a microfiber may assume a barrel- or clamshell-shaped morphology, which depends upon the fiber diameter, droplet volume and contact angle. McHale et al. (2001, 2002) have determined the critical droplet volume for the morphology transition between barrel- and clamshell-shaped droplets wetting on filaments at varying contact angle by using SFEM (Brakke, 1992; Brakke, 2000). McHale and his coworkers' predictions were well correlated to the roll-up condition by Carroll (Carroll, 1986) and their experimental observations (McHale et al., 2001; McHale et al., 2002). By extending McHale's works (McHale et al., 2001; McHale et al., 2002), Chou et al. (2011) further considered the effect of gravity on the morphology transition of droplet-on-filament between the barrel and clamshell shapes, and their numerical simulations indicated that the stable droplet volume is

noticeably decreased by gravity. Similarly, de Ruiter et al. (2012) studied the morphology transition of buoyant droplets on a filament using a well controlled electrowetting setup.

Beyond monolithic droplets wetting on a filament, several works have also been performed to understand the wetting and spreading behavior of a droplet sitting on multiple fibers. Among others, Princen (1969a; 1969b; 1970) first considered the simplest cases of wetting and spreading of liquids in aligned multi-fiber systems, in which an asymptotic analysis was explored for determining the capillary rises and wetting lengths in two and multiple vertically/horizontally-positioned filaments. Keis et al. (2004) indicated the potential of utilizing a pair of parallel microfibers to manipulate small quantity of liquids in micro liters. Their measurements showed that the wicking kinetics of a droplet spreading on such a fiber pair roughly obeyed the Lucas-Washburn law (Lucas, 1918; Washburn, 1921) such that given a fiber spacing, the growing wetting length of the meniscus is proportional to the complete wicking time (*i.e.*, the time interval from the start of droplet spreading to its disappearance). Yet, a droplet sitting on a pair of two parallel fibers may assume a barrel-shaped droplet, which completely enwraps the two fibers, or a liquid bridge, which only partially wets the internal surfaces and therefore partially enwraps the two fibers. Such a morphology transition could further influence the liquid spreading. Similar to the work by McHale et al. (2001; 2002), Wu et al. (Wu et al. 2010; Bedarkar et al., 2010) determined the characteristic wetting curves as the phase diagram boundaries between the morphologies of barrel-shaped droplet and liquid bridge spanning on two aligned filaments. Based on controlled droplet-on-fiber systems, Protiere et al. (2013) recently identified such a morphology transition based on an experimental morphology diagram and discovered the transition hysteresis, a wetting phenomenon commonly observed in droplet spreading. In addition, Bedarkar and Wu (2009) and Virozub et al. (2009) determined the

capillary torque induced by a droplet bridge formed between two misaligned filaments, where symmetry breaking of a droplet bridge triggers the non-symmetric capillary force that is responsible for the capillary torque.

Moreover, the capillary force due to droplets wetting and spreading on filaments may also result in noticeable elastic deformation, i.e., elastocapillary effect, which further influences the interaction between the droplets and filaments (Wu, 2010; Bico et al., 2004; Boudaoud et al., 2007; Aristoff et al., 2011; Duprat et al., 2011; Duprat et al., 2012; Beukirch et al., 2007; Hure et al., 2013; Liu et al., 2012; Roman et al., 2010). Such an elastocapillary effect could be exploited for assembly of microdevices (Syms et al., 1999; Syms et al., 2003; van Honschoten et al., 2010). The capillary force due to liquid wetting and spreading in fiber networks may also lead to fiber collapse, contact and fusion (Wu and Dzenis, 2007; Wu et al., 2012; Wu and Dzenis, 2005), which further affect the mechanical response of fiber networks.

2.3.2. Outstanding Problems

Yet, all the above studies were focused on a homogeneous droplet wetting on a monofilament or multi-fibers. To author's knowledge, no systematic studies have been reported yet in the literature on dissimilar liquids wetting on filaments though such phenomena are also typically observed in nature and engineering activities such as cleaning of water/oil mixture on textiles, sorption and recovering of ocean oil-spill, etc. Thus, as a natural extension of the above works on wetting and spreading of homogeneous droplets on fibers and filaments, in this work we initiate the theoretical study on determining the surface morphology and surface energy of two immiscible micro-droplets wetting and engulfing on a filament. A set of coupled governing ordinary different equations (ODEs) will be formulated and solved in closed form. In parallel, a computational microfluidic model of the current problem will be established and solved by

means of SFEM (Brakke, 1992; Brakke, 2000), which will be used to validate the analytic solutions. Dependencies of the droplet morphology and surface energy upon the droplet surface properties, contact angle, droplet volume, and filament diameter will be examined. Discussions on the results and potential applications of research will be addressed consequently.

2.4. Surface Evolver

Surface Evolver (Brakke, 1992; Brakke, 2000) was employed in this study for determining the wetting morphology, surface energy and capillary force exerted by a droplet, liquid bridge, or mixture of two or more liquids, which is a free computational microfluidic software package available online. By means of surface finite element method (SFEM), *Surface Evolver* was developed by Brakke (1990, 2000) to find the minimum surface area via minimizing the surface energy of the liquid surface with given volume, which is defined by various constraints, which are set by the program or the users. The surface is represented as a simplicial complex. The liquid energy can include the surface tension, gravity or any other forms or attributes that are natural. Constraints can be geometrical constraints on vertex positions or constraints on integrated quantities such as body volumes. The minimization is done by evolving the surface down the energy gradient (Brakke, 1992; Brakke, 2000).

2.4.1. Original Surfaces

The original surfaces are the surfaces forming the very beginning of the droplet profile. In *Surface Evolver*, these surfaces are defined with respect to the geometric elements in each dimension. In each element, there are a series of attributes to determine the element. These attributes are open and allow users to define the extra attributes in the Input Data File. Elements that form the final droplet model are the most fundamental geometric elements including Vertices, Edges, Facets and Bodies.

2.4.1.1. Vertices

Like other finite element analysis (FEA) packages, SFEM is also ruled in terms of space, which means a vertex is a point that belongs to this space. A critical difference exists by comparison with other finite element methods (FEM) such that the vertex coordinate in SFEM is varying with the evolution of the surfaces in each numerical iteration, which could be understood as a process of self-adaptive mesh refinement.

2.4.1.2. Edges

Edges in *Surface Evolver* are defied as the one-dimensional (1D) geometrical element to connect two neighboring Vertices. Edges of original surfaces are defined according to vertices previously defined in Input Data file.

2.4.1.3. Facets

Due to the requirement of evolution process, facets must be in triangle mode, each of which is formed by three edges. Edges are usually defined in the previous step. Yet, some of them may not be defined in advance and they can be automatically formed according to the evolution. Thus, in a process of numerical evolution of a droplet surface, the surface can always be refined in triangles with the facet area smaller and smaller. This method ensures the refinement in an accurate way. When speaking of energies, most of energies are distributed to vertices and edges. The energies cannot be defined externally because of the rules of formatting principles, but they can carry extra energies by naming quantities that applied to them.

2.4.1.4. Bodies

Body in *Surface Evolver* is closed volumetric geometrical body which is formed by several facets. Body is the final format and is also the full dimension of a droplet model in space.

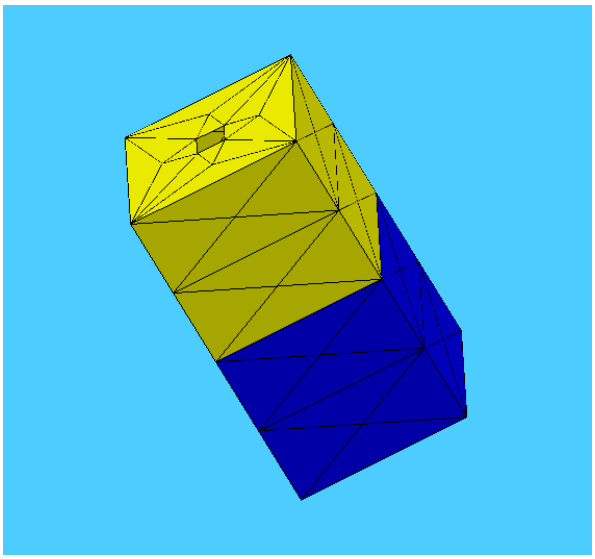

Figure 2.10. Shows the schematic of an original structure

2.4.2. Energies

To a great extent, energies are the quantities that the SFEM is used to minimize, which are expressed in terms of integrals with respect to surfaces. The most common energy is surface tension which is defined as force per unit length. Surface tension exists for any surface, which is equal to the surface energy density. Surface tension can be specified by the users in any facet they want. Gravitational potential energy is another energy that is usually considered in simulation, which can be distributed by mean of divergence theorem in terms of integrals. However, when the droplet size is smaller than the capillary length (around a few millimeters for water), the effect of gravity can be safely ignored.

If the mass density of a body is assumed as ρ and the gravity is defined along opposite *z*-axis, the resulting gravitational potential energy in the body can be expressed as

$$E = G\rho \iiint z dV \tag{2.12}$$

where *G* is the acceleration of gravity, which can be user-defined for scaling purpose.

According to the divergence theorem, relation (2.12) can be recast as

$$E = G\rho \iint \frac{z^2}{2} \vec{k} d\vec{S} \tag{2.13}$$

which transfers the energy from a volume integral into a surface integral. The above transfer simplifies the energy calculation such that the summation of facets bounding the liquid body leads to the total energy of an entire surface. In special case, when one facet is occupied by two bodies of different densities, different densities can be defined simultaneously on both side of the facet.

2.4.3. Constraints

There are two types of constraints for minimizing energies. One type takes place on the motion of vertices and the other takes place on the value of surface integrals. As aforementioned, vertices can be independently constrained through defining them as fixed or by defining their location in terms of parameters. Constraints contain boundaries, volumes and quantities. Quantities are usually called surface integrals.

2.4.4. Working Principles

The key process of SFEM in *Surface Evolver* is the numerical iteration, through which the program gradually minimizes the surface energy while maintaining the defined constraints. A gradient descent method is utilized in the minimization process. A general series of command set of the evolution iterations is exemplified in Figure 2.11 as below

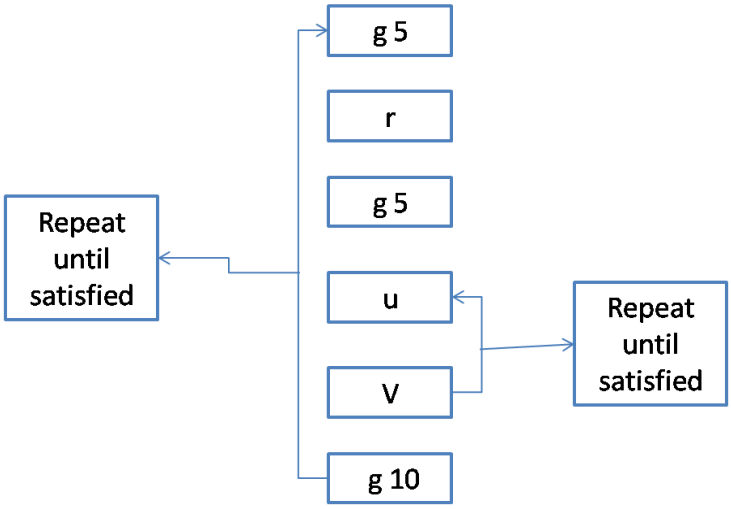

Figure 2.11. General commands and loop of evolution steps

2.5. Oil-Water Separation

2.5.1. Significance

Oil resource plays an important role in the development of human society, especially in the modern industrial development. Accidents of oil-spill and oil leakage often happen due to careless operations, transportation, storage and utilization. The most disastrous oil-spill happened in the Gulf of Mexico in 2010, which has caused a set of problems both to the ocean ecosystem and human society. To the ocean, it has a huge negative impact on the wildlife and habitats. For example, ocean creatures such as dolphins are going to die when the water surface is covered by a very thick face, which will be breathed into their breathing system through the blowholes and lead them to death. Sea turtles feeding on small fishes and planktons are also in danger in oil-polluted ocean. When sea turtles eat oil-covered foods, oil enters their mouth which is further ingested by their organs and hurts the internal organs of sea turtles. Sea birds catch fishes by diving into water and their feathers can be easily contaminated by oil due to the oleophilic nature of bird feathers. Once the feathers are covered by oil, a failure of flying causes their death.

To human beings, it would be a disaster to economy. For example, the tourism, beaches are all closed because the contamination of sands, and also the coastal water, which can be harmful to human body's health. And also, to the trade of seafood, it is also having big impact because of the pollution. Thus, effective strategies and methods to get rid of oil in water can be an urgent challenge to human. The most common way nowadays to deal with oil spill is to pour chemical dispersants into water which can break down the oil slicks. Yet, since the method based of chemical dispersant is to use one chemical to treat a second one, it unavoidably causes side effort or other serious environmental problems (Foxnews, 2010). For instance, pouring specific chemical into seashore may result in the rapid growth of sea plants and planktons. To date, quite a few new materials have been invented and produced such as exfoliated carbon (graphite), carbon nanotubes (CNTs), non-polar polymer fibers, clay, silica aero-gel, acetylated rice straw (Xue et al., 2013) and so on. However, disadvantages of these oil-sorption materials are still so obvious. Firstly, the current oil-sorption materials cannot be largely applied to the accident region like oil-spilled ocean. Secondly, the oil-sorption capability and efficiency of these materials are still low and second pollution may be caused due to the poor recyclability. Therefore, low-cost, efficient oil-spill sorption and oil-water separation techniques are highly demanded for environmental protection and remedy

CHAPTER 3. WETTING ANALYSIS OF A LIQUID BRIDGE SYSTEM

3.1. Introduction

Liquid bridge is a phenomenon that a liquid droplet is formed between two solid surfaces due to surface tension. Adhesion force occurs in the contact area between liquid and solid surfaces (Honschoten, 2009). In addition, in the study of oil-water separation, it is important to understand and differentiate the adhesion force between a droplet of water or oil and the solid surface. The capillary force exerted by liquid bridge also dominates the wetting and dewetting phenomena in porous materials such as micro/nanofibrous materials used for oil-water separation. For a liquid bridge system, several physical characteristics can be identified, which are the important parameters used for characterizing the wetting and dewetting behavior of liquids. In order to understand the wetting behavior of a liquid bridge, the theoretical background of liquid bridge is revisited and the governing ODE is refined and used for extracting the wetting parameters. In addition, detailed numerical simulation has been performed to examine the effects of surface properties and plate spacing on the capillary pressure and adhesion force of the liquid bridge between two flat plates. The critical adhesion force at the breakage of a liquid bridge between two flat surfaces was determined at varying surface wetting properties (e.g., contact angles). *Surface Evolver* was used for the numerical simulation.

3.2. Problem Formulation

A small quantity of liquid placed between two surfaces forms a liquid bridge. To date, a significant number of analytical and experimental approaches to liquid bridges have been reported in the literature (Yao, 1998; Wei, 2007; Fan 2001; He, 2001). Yet, many descriptions are based on some extent of theoretical approximation, which do not exactly represent the actual physical observations. In this chapter, a new mathematical formulation is employed to describe

the morphology and adhesion force of a droplet bridge between two flat surfaces. SFEM is further used to determine the characteristic parameters of the droplet bridge including the surface energy, wetting area (radius), and adhesion force. Their dependencies upon the surface spacing are examined numerically in detail.

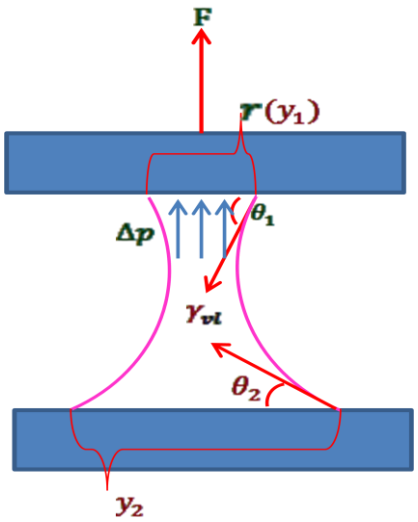

Figure 3.1. Schematic diagram of a liquid bridge forms between two surfaces with dissimilar wetting properties. Contact angle θ_1 refers to the upper contact area and contact angle θ_2 refers to the lower contact area

3.2.1. Mathematical Model

Consider a microscale liquid bridge formed between two flat plates with different wetting properties as shown in Figure 3.1. Herein, the gravity effect is ignored, thus the capillary force is the dominant factor governing the morphology evolution of a liquid bridge as described by Young-Laplace equation:

$$\Delta P = \gamma\left(\frac{1}{R_1}+\frac{1}{R_2}\right) \tag{3.1}$$

For axisymmetric capillary problems such as liquid bridges, barrel-shaped drops wetting on fibers, the corresponding Young-Laplace equation can be expressed (Wu and Dzenis, 2006):

$$\frac{1}{y(x)\sqrt{1+\left[y'(x)\right]^2}}-\frac{y''(x)}{\sqrt[3]{\left\{1+\left[y'(x)\right]^2\right\}^2}}=\frac{\Delta P}{\gamma} \tag{3.2}$$

where ΔP is the capillary pressure, and γ is the surface tension. Eq. (3.2) is a 2nd order ODE, and two boundary conditions are specified:

$x = 0$

$$y_0' = -\tan\left(\frac{\pi}{2}-\theta\right) = -\cot\theta_1 \tag{3.3}$$

$x = L$

$$y_L' = \cot\theta_2 \tag{3.4}$$

It can be found that a first integral to Eq. (3.2) can be identified (Wu and Dzenis, 2006)

$$\frac{1}{\sqrt{1+\left[y'(x)\right]^2}} = Ay(x) + B/(y) \tag{3.5}$$

where A and B are unknown constants to be determined and A has the relation

$$A = \frac{\Delta P}{\gamma} \tag{3.6}$$

Substitution of the two boundary conditions (3.3) and (3.4) into the first integral (3.5) yields

$$\sin\theta_1 = Ay_1 + By_1 \tag{3.7}$$

$$\sin\theta_2 = Ay_2 + By_2 \tag{3.8}$$

Thus, the constants A and B in (3.7) and (3.8) can be determined by solving the above set of linear algebraic equations:

$$A = \frac{y_1\sin\theta_1 - y_2\sin\theta_2}{y_1^2 - y_2^2} \tag{3.9}$$

$$B = \frac{y_1 y_2 \left(y_1 \sin\theta_2 - y_2 \sin\theta_1 \right)}{y_1^2 - y_2^2} \tag{3.10}$$

Expression (3.9) indicates that A can be expressed in terms of the radii of contact areas y_1 and y_2, which can be measured in experiments.

With the expressions of A and B in relations (3.9) and (3.10), the capillary pressure of the liquid bridge is

$$\Delta P = \frac{2\gamma \left(y_1 \sin\theta_1 - y_2 \sin\theta_2 \right)}{y_1^2 - y_2^2} \tag{3.11}$$

Finally, plug the capillary pressure ΔP in to the first integral (3.5), it reads

$$y'' + \frac{2\left(y_1 \sin\theta_1 - y_2 \sin\theta_2 \right)}{y_1^2 - y_2^2} \sqrt[3]{\left\{ 1 + \left[y'(x) \right]^2 \right\}^2} - \frac{1 + \left[y'(x) \right]^2}{y(x)} = 0 \tag{3.12}$$

In addition, the adhesion force (2.11) can be recast as

$$F = 2\pi y_1 \gamma \sin\theta_1 - \frac{2\gamma \left(y_1 \sin\theta_1 - y_2 \sin\theta_2 \right)}{y_1^2 - y_2^2} \pi y_1^2 \tag{3.13}$$

In this study, we were not interested in solving the above governing nonlinear ODE; however, it was used to derive the modified adhesion force (3.13) for determining the numerical adhesion force based on the SFEM simulations.

3.3. Numerical Simulation

Hereafter, SFEM was utilized to minimize the total surface energy of a liquid bridge in order to evolve the morphology of a real liquid bridge. During a SFEM-based simulation, at the instant when the total surface energy is minimized, the shape of a liquid bridge in nature is obtained. Four cases were simulated in this study: Two symmetric models with contact angle of 30 and 40 degrees, two asymmetric models with the upper contact angles of 60 and 120 degrees and the lower contact angles of both 30 degrees, respectively. Below figures show two different

models that are evolved by the same steps. Here the evolution processes of two cases of liquid bridge are shown. Figure 3.2 is a symmetric liquid-bridge model built using SEFM tool, where the contact angles are selected as 40 degrees on both the contact areas. Figure 3.3 shows an asymmetric liquid bridge model with the upper contact angle of 60 degree and the lower contact angle of 30 degree.

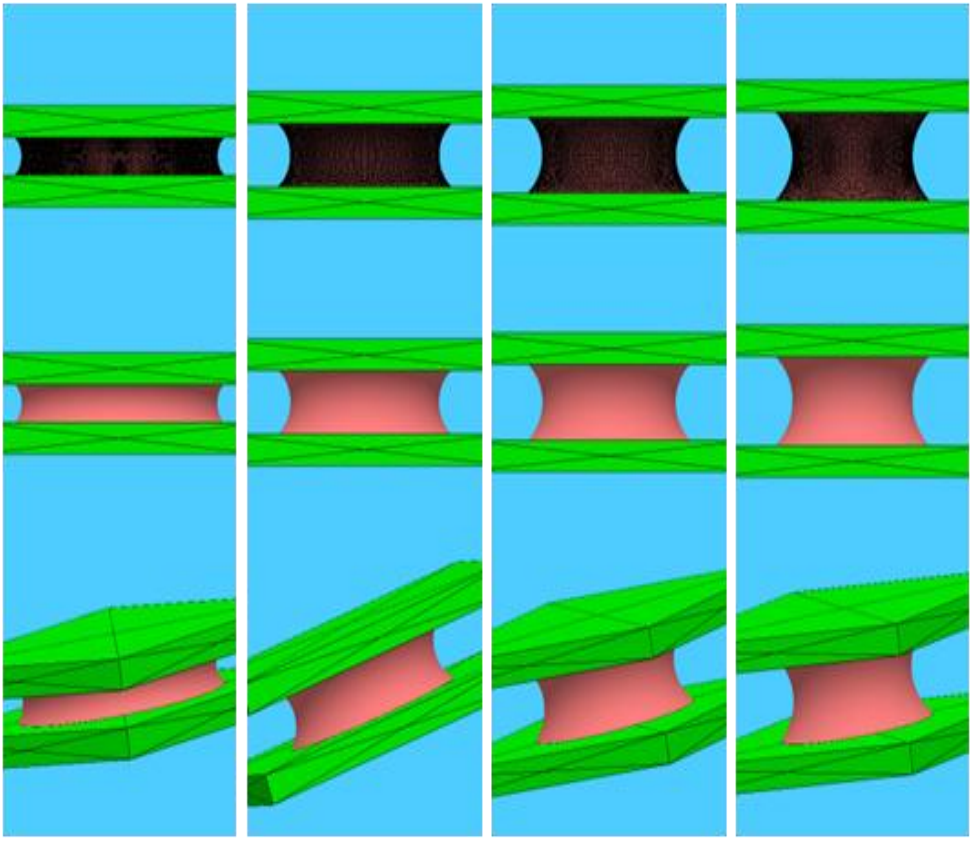

(*a*) (*b*) (*c*) (*d*)

Figure 3.2. Snapshots of the morphology evolution at varying plate spacing. The contact angle of the upper and lower plates are fixed at 40^{o}; the dimensionless liquid volume is fixed as 1; the dimensionless surface tension is fixed as 1

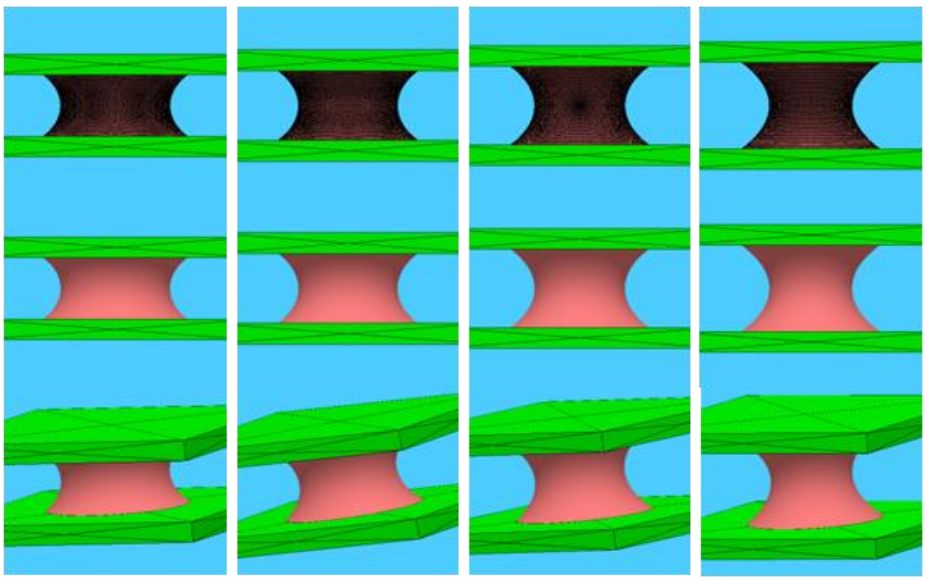

(*e*) (*f*) (*g*) (*h*)

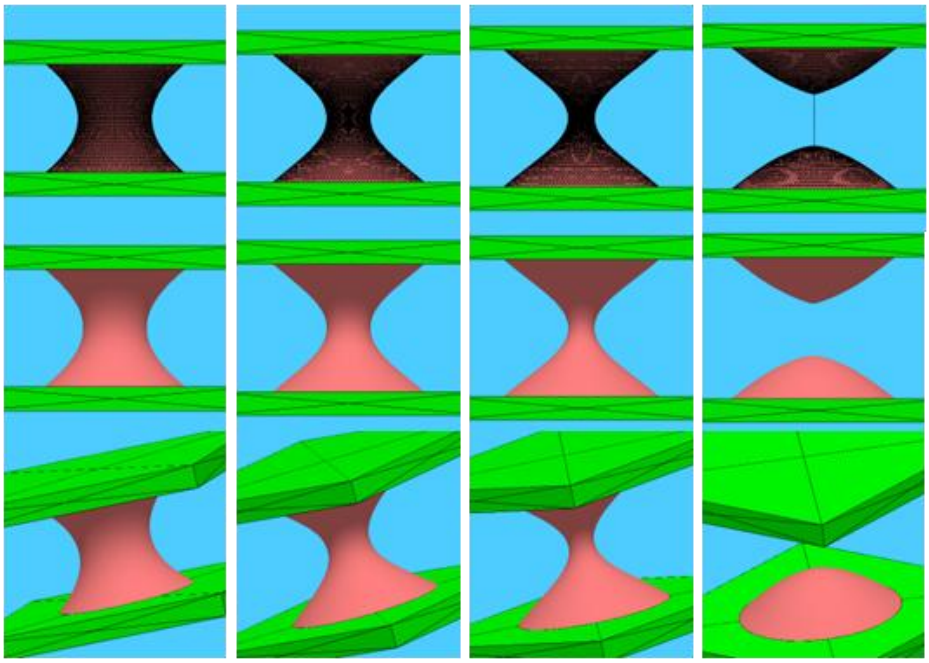

(*i*) (*j*) (*k*) (*l*)

Figure 3.2. Snapshots of the morphology evolution at varying plate spacing. The contact angle of the upper and lower plates are fixed at 40^{o}; the dimensionless liquid volume is fixed as 1; the dimensionless surface tension is fixed as 1(continued)

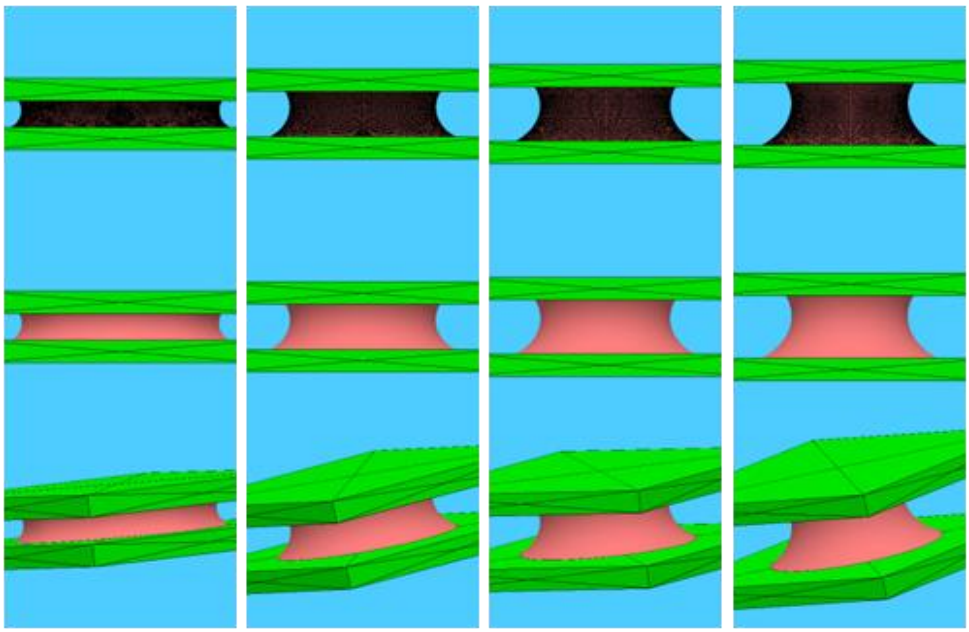

(*a*) (*b*) (*c*) (*d*)

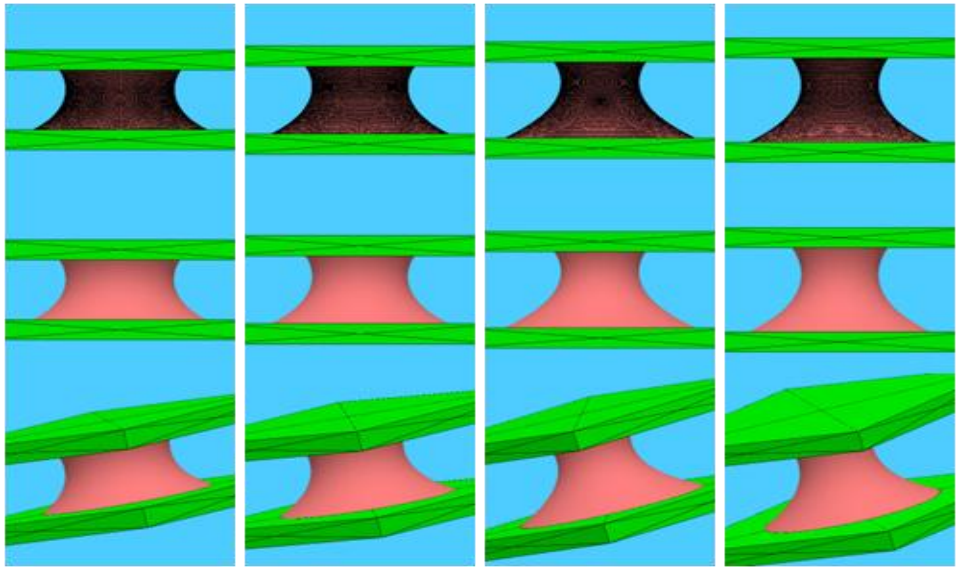

(*e*) (*f*) (*g*) (*h*)

Figure 3.3. Snapshots of the morphology evolution at varying plate spacing. The contact angles of the upper and lower plates are fixed at 60^{o} and 30^{o}, respectively; the dimensionless liquid volume is fixed as 1; the dimensionless surface tension is fixed as 1

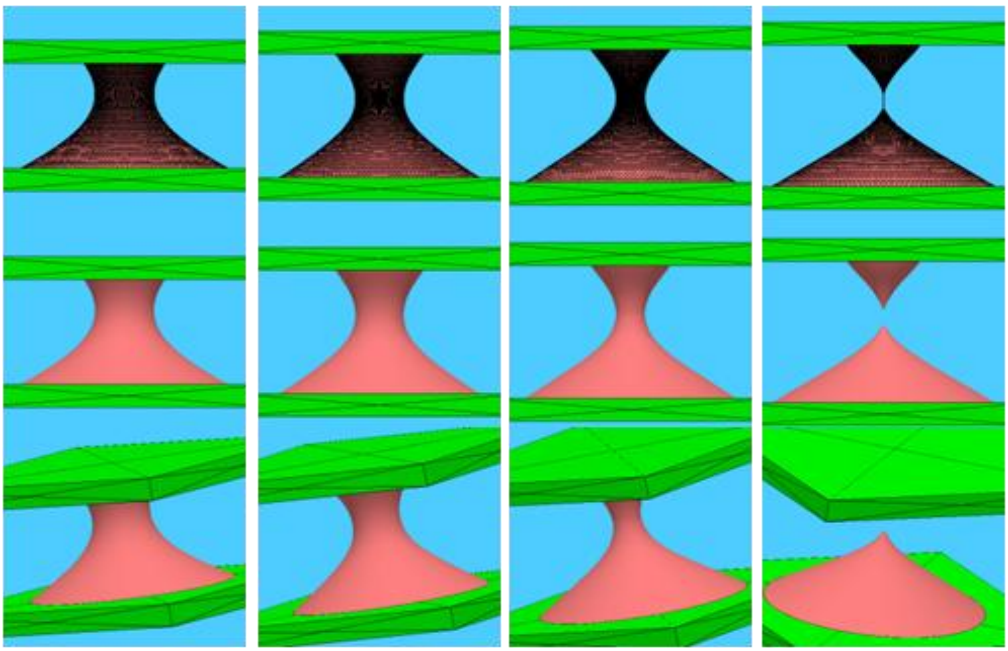

(*i*) (*j*) (*k*) (*l*)

Figure 3.3. Snapshots of the morphology evolution at varying plate spacing. The contact angles of the upper and lower plates are fixed at 60^{o} and 30^{o}, respectively; the dimensionless liquid volume is fixed as 1; the dimensionless surface tension is fixed as 1(continued)

3.4. Results and Discussion

With the above numerical simulations, the characteristic curves of liquid bridges can be extracted accordingly. The adhesion forces were extracted from the numerical results of SFEM by using relation (3.13). Variations of the adhesion force of liquid bridge with respect to the plate spacing h in the four modeling cases are shown in Figure 3.4. From Figure 3.4, it can be observed that in all the above modeling cases, the adhesion force of liquid bridge decreases with increasing plate spacing until the breakage of liquid bridge. In the first three cases, the zero adhesion force after breakage of the liquid bridge was not plotted in the figures. In addition, the liquid bridge in these three cases broke into two droplets attached to the upper and lower surfaces, respectively, due to the hydrophilic nature of the surfaces.

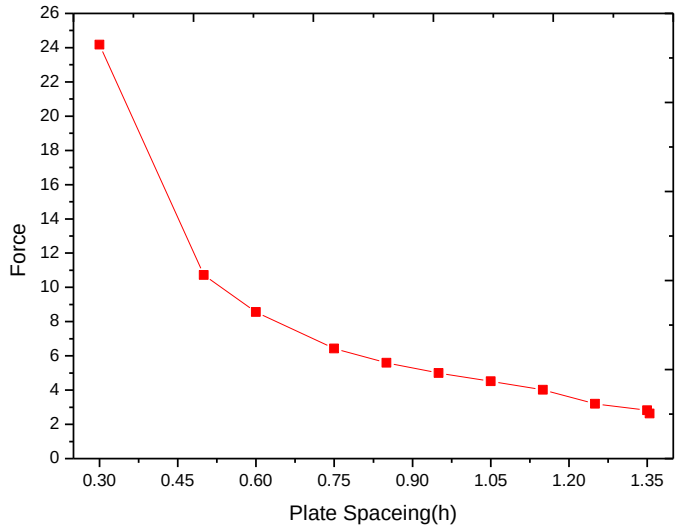

(*a*)

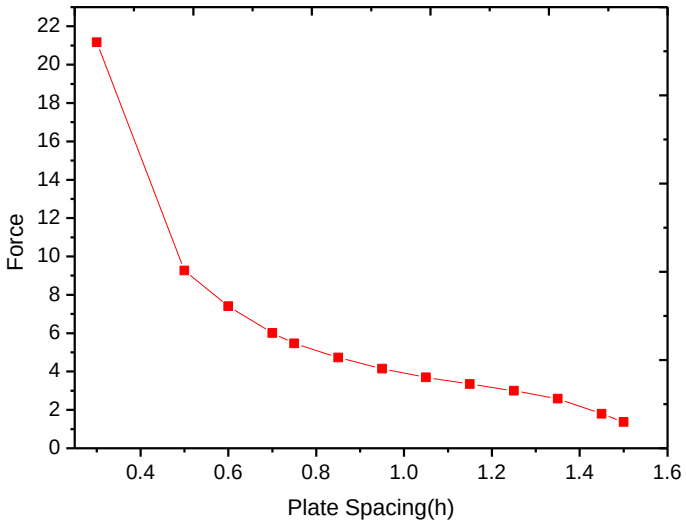

(*b*)

Figure 3.4. Variation of the adhesion force with the plate spacing in four surface wetting cases. The two curves marked as (*a)* and (*b)* are axisymmetric models with the contact angle of 30 and 40 degrees. The two curves marked as (*c)* and (*d)* are asymmetric models with the upper contact angles of 60 and 120 degrees and the lower contact angles of both 30 degrees, respectively

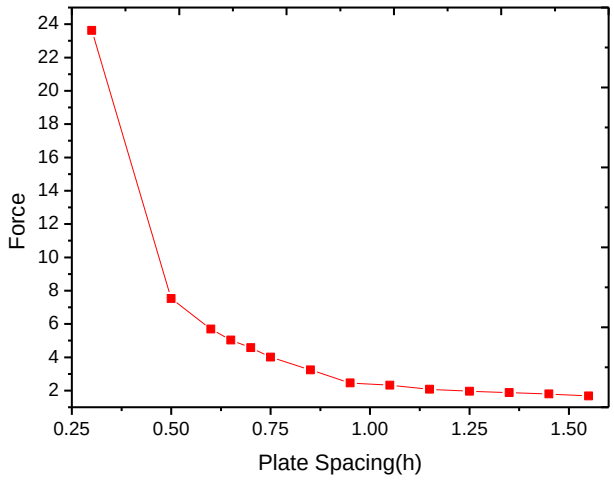

(*c*)

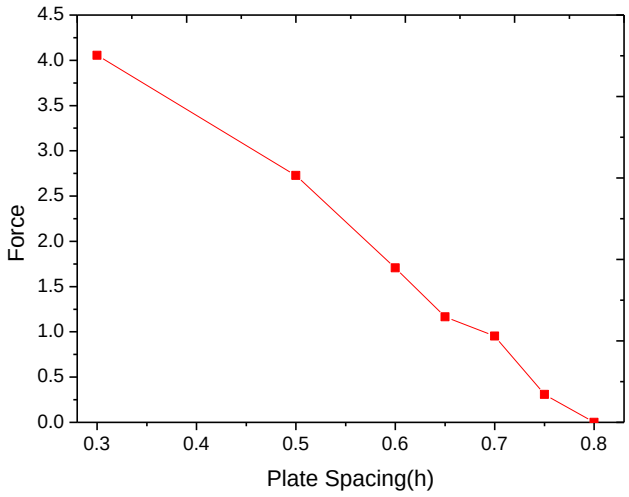

(*d*)

Figure 3.4. Variation of the adhesion force with the plate spacing in four surface wetting cases. The two curves marked as (*a)* and (*b)* are axisymmetric models with the contact angle of 30 and 40 degrees. The two curves marked as (*c)* and (*d)* are asymmetric models with the upper contact angles of 60 and 120 degrees and the lower contact angles of both 30 degrees, respectively (continued)

Figure 3.5 show the variations of the capillary pressure with respect to the plate spacing. It can be observed from Figure 3.5 that in each case, the capillary pressure increases until the liquid bridge breaks. In addition, it is also found that the capillary pressure starts from a negative value to a positive. This observation is due to the fact that one of the radii of curvature changes its sign during the entire range of plate spacing in the numerical experiment according to Young-Laplace equation,

$$\Delta P = \gamma\left(\frac{1}{R_1}+\frac{1}{R_2}\right), \tag{3.14}$$

In this case, when the absolute value of R_1 (with the negative sign, i.e., outward curvature) is much smaller than the absolute value of R_2 (with the position sign – inward curvature), the value of ΔP turns out negative. On the contrary, if the absolute value of R_1 is much larger than the absolute value of R_2, the value of ΔP becomes positive.

In the below all numerical experiments, dimensionless parameters have been used. The resulting curves are the characteristic properties of a family of liquid bridges, which can be used for scaling analysis of the wetting behavior of liquid droplet bridging two plates and extracting the data. Figure 3.6 shows variations of the wetting size (radius of wetting area) with respect to the plate spacing for four cases of different surface wetting properties. In Figure 3.6, cases (*a*) and (*b*) are the numerical results based on the assumption of the same plate wetting properties. It can be found that in each case, with the increase of the plate spacing, the radius of wetting area first decreases to a stationary point and grows up. This observation could be explained such that since the substrates are hydrophilic, the breakage of liquid bridge beyond the critical plate spacing happens inside the liquid.

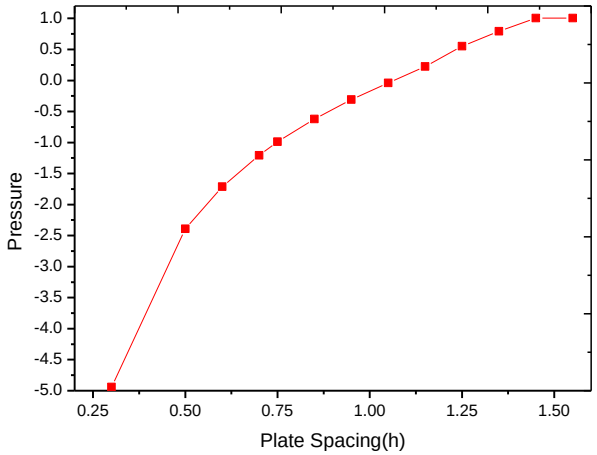

(*a*)

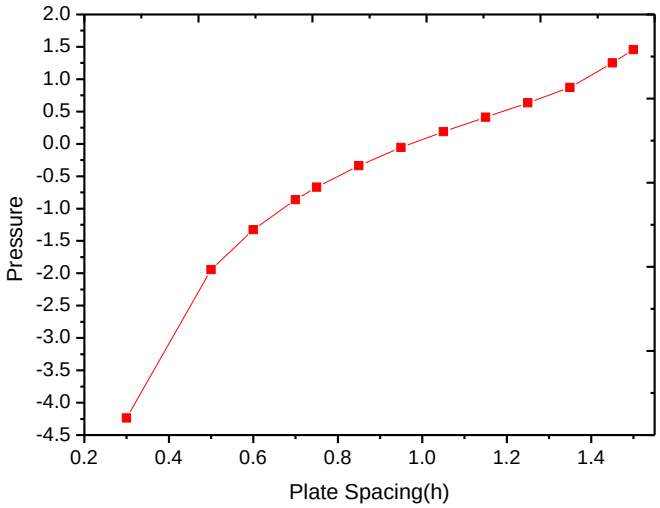

(*b*)

Figure 3.5. Variation of the capillary pressure with respect to the plate spacing in four cases of plate wetting properties. Cases *(a)* and *(b)* are symmetric models with the contact angles of 30 and 40 degrees, respectively; Cases *(c)* and *(d)* are asymmetric models with the upper contact angles of 60 and 120 degrees and the lower contact angles of both 30 degrees, respectively

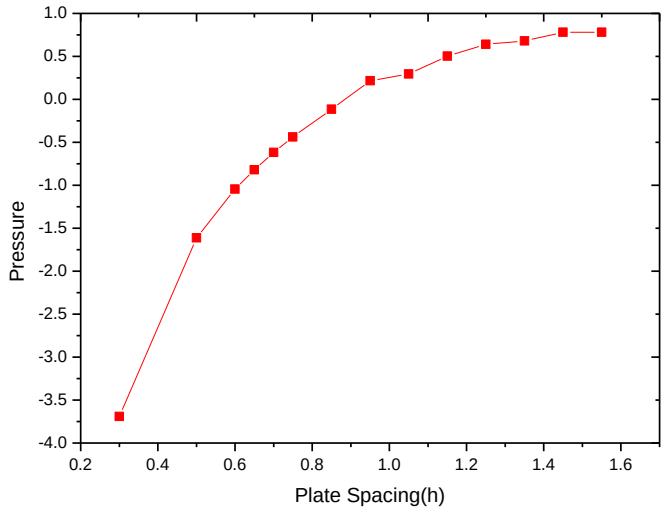

(*c*)

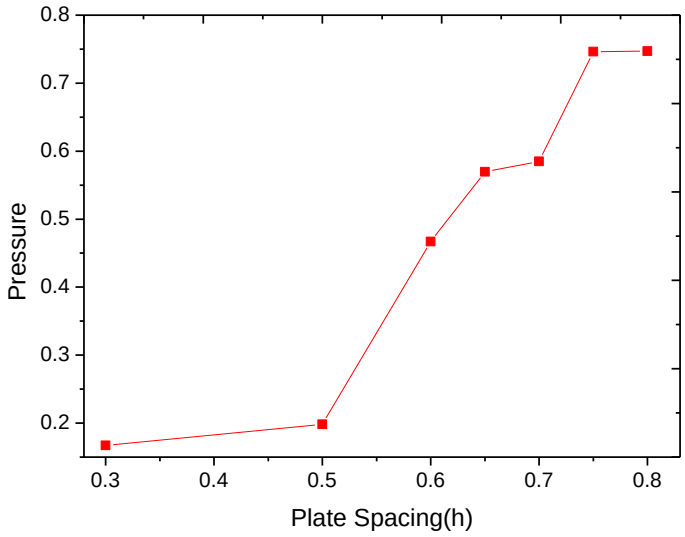

(*d*)

Figure 3.5. Variation of the capillary pressure with respect to the plate spacing in four cases of plate wetting properties. Cases *(a)* and *(b)* are symmetric models with the contact angles of 30 and 40 degrees, respectively; Cases *(c)* and *(d)* are asymmetric models with the upper contact angles of 60 and 120 degrees and the lower contact angles of both 30 degrees, respectively (continued)

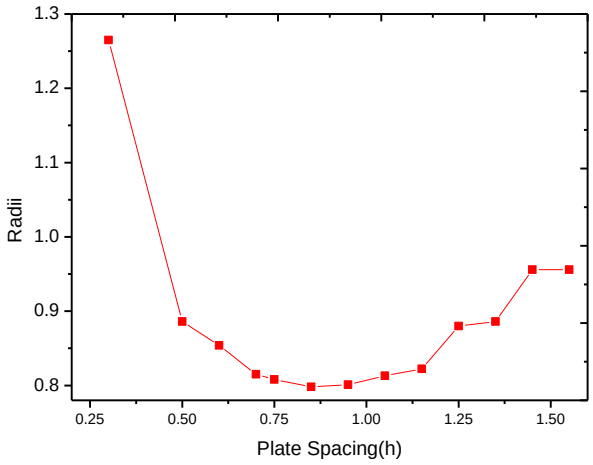

(*a*)

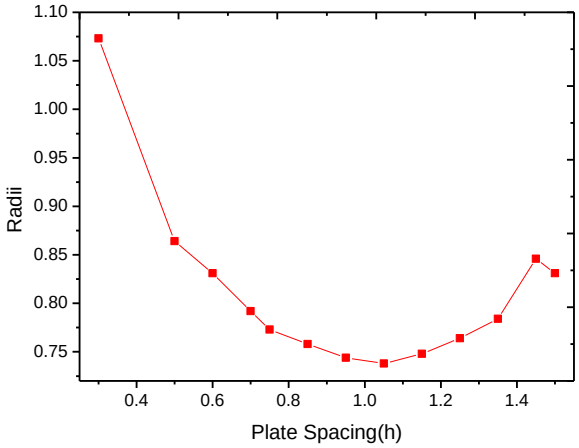

(*b*)

Figure 3.6. Variation of the radius of upper wetting area with respect to the plate spacing for the four models. Curves marked as *(a)* and *(b)* are the axisymmetric models with contact angle of 30 and 40 degrees; curves marked as *(c)* and *(d)* are *a*symmetric models with the upper contact angles of 60 and 120 degrees and the lower contact angles of both 30 degrees

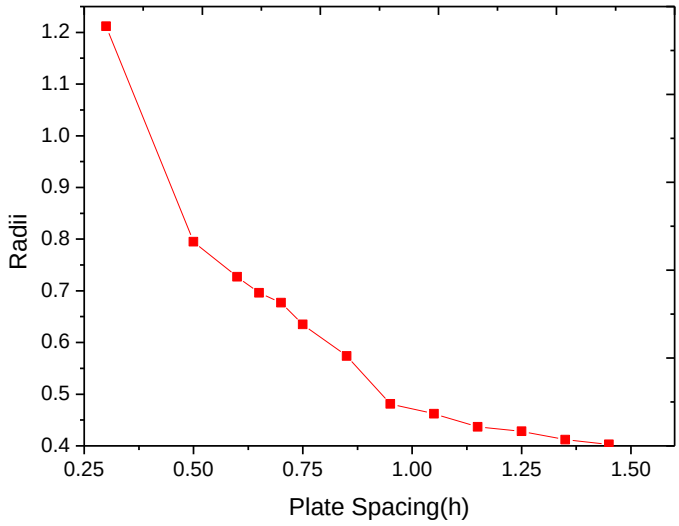

(*c*)

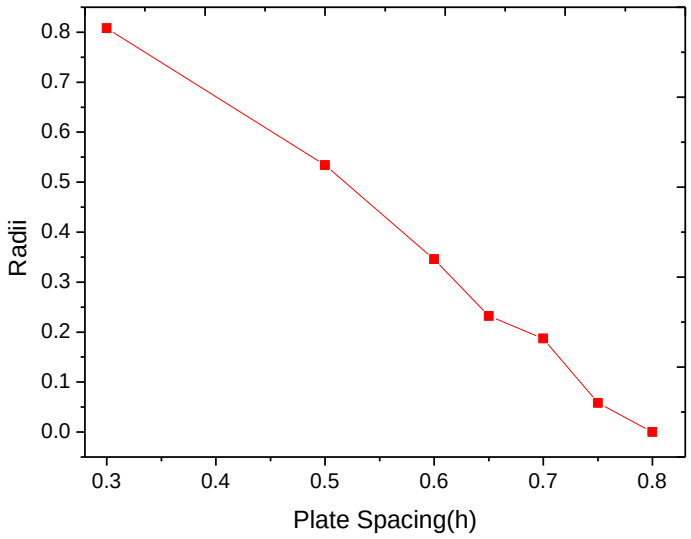

(*d*)

Figure 3.6. Variation of the radius of upper wetting area with respect to the plate spacing for the four models. Curves marked as *(a)* and *(b)* are the axisymmetric models with contact angle of 30 and 40 degrees; curves marked as *(c)* and *(d)* are *a*symmetric models with the upper contact angles of 60 and 120 degrees and the lower contact angles of both 30 degrees (continued)

3.5. Summary

The adhesion force induced by a liquid bridge between two parallel, flat plates has been analyzed under varying wetting situations including the upper and lower plates with the same and dissimilar contact angles, respectively. In addition, capillary pressures and radius of wetting area of the liquid bridges at varying plate spacing are obtained. The present numerical experiments indicate that the adhesion force varies in the same trend in either the same or dissimilar wetting surfaces. In other words, the adhesion force always decreases with increasing plate spacing. The capillary pressure behaves as increasing with the increase of plate spacing during the whole evolution process. While, in terms of the radius of wetting area, the situation is different. It can be observed that when the liquid bridge forms between two same plates, the radius of wetting area has a valley point (stationary point) between two extreme ends. The radius of wetting area decreases with the plate spacing before the stationary point, and then increases with the plate spacing until the bridge breaks.

CHAPTER 4. DROPLETS ENGULFING ON A FILAMENT

4.1. Introduction

This chapter studies the engulfing behavior of two immiscible droplets contacting and sitting on a filament. Two immiscible droplets wetting on a filament may assume engulfing, partial-engulfing, or non-engulfing morphology depending on the wetting behavior and geometries of the droplet-on-filament system. A set of ODEs is formulated for determining the morphology of the droplet-on-filament system. In the limiting cases of engulfing and non-engulfing, the morphologies of the droplet-on-filament system are determined in explicit expressions. In the case of partial engulfing, SFEM-based *Surface Evolver* is employed for determining the droplet morphology, surface energy, and capillary pressures of droplets of the system. Numerical scaling studies are performed to explore their dependencies upon the wetting properties and geometries of the system. The study can be applicable for analysis and design of tailorable wetting properties of textiles and development of novel multifunctional fibrous materials for environmental protection such as oil-spill sorption, etc.

4.2. Problem Formulation

4.2.1. General Governing Equations

Consider two immiscible droplets partial-engulfing axisymmetrically on a filament of uniform circular cross-section as shown in Figure 4.1(*b*). Figure 4.2 is the corresponding schematic diagram with a proper coordinate system. For the convenience of derivation hereafter, except for those designated specifically, parameters and variables with subscripts “1”, “2”, and “12” are attached to droplet 1, droplet 2, and the interface between droplets 1 and 2, respectively, Due to the axisymmetry of the droplet-on-filament system, the principal radii R_1 and R_2 of curvature of each droplet surface of the droplets at locus $[x, y(x)]$ can be expressed:

$$1/R_1 = 1/(y\,\mathrm{cosec}\,\psi) = 1/[y(x)\sqrt{1+[y'(x)]^2}] \tag{4.1}$$

$$1/R_2 = -y''(x)/\sqrt{\{1+[y'(x)]^2\}^3} \tag{4.2}$$

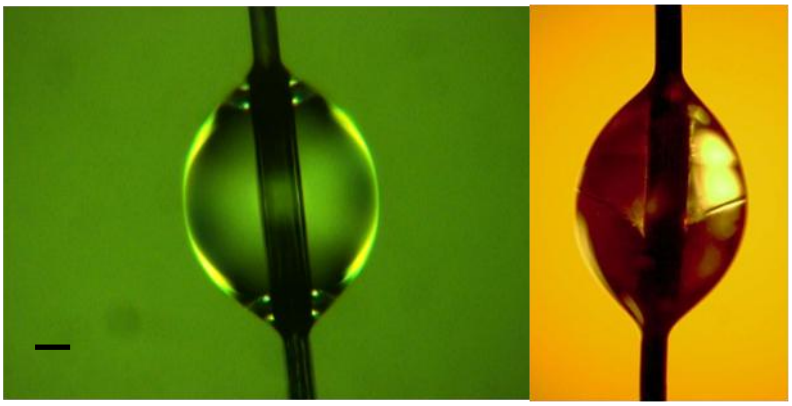

(*a*) (*b*)

Figure 4.1. Optical micrographs of (*a*) a barrel-shaped epoxy droplet wetting on a carbon fiber and (*b*) two immiscible droplets of polyacrylonitrile (PAN)-N,N-dimethylformamide (DMF)/isophorone diisocyanate (IPDI)-DMF partial-wetting on a carbon fiber (with the visible interface at the middle)

Thus, Young-Laplace formula specified the surface morphology of the liquid droplets **(**de Gennes, 2004; Starov et al., 2007; Wu and Dzenis, 2006), which reads

$$\gamma(1/R_1 + 1/R_2) = \Delta P \tag{4.3}$$

where ΔP is the droplet pressure defined as

$$\Delta P = p_L - p_V \tag{4.4}$$

In the above, p_L and p_V are the pressures inside and outside the droplet, respectively. As a result, the governing ODE for each curvilinear segment of the droplet profile can be obtained by substituting (4.1) and (4.2) into (4.3) such that

$$\gamma\{1/\{y(x)\sqrt{1+[y'(x)]^2}\} - y''(x)/\sqrt{\{1+[y'(x)]^2\}^3}\} = \Delta P \tag{4.5}$$

As discussed in Chapter 3, Eq. (4.5) has a first integration:

$$1/\sqrt{1+[y'(x)]^2} = Ay(x) + B/y(x) \tag{4.6}$$

where

$$A = \Delta P/(2\gamma) \tag{4.7}$$

and B is an integration constant which can be determined according to the contact angle at the droplet end.

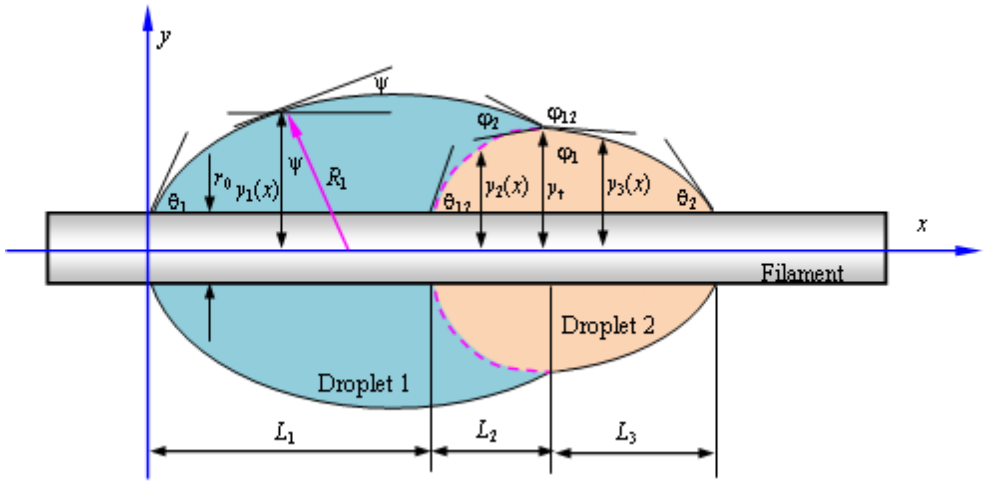

Figure 4.2. Geometries of two immiscible droplets partial-engulfing axisymmetrically on a filament

In addition, there are three boundary conditions (BCs) of contact angle at the right, internal and left ends of the droplets and one three-phase intersection condition at the outer surface, which are specified as shown in Figure 4.3. The three-phase intersection of droplet/droplet/gas shown in Figure 4.3(*c*) gives (Hudson, 1998)

$$\frac{\sin\varphi_1}{\gamma_1} = \frac{\sin\varphi_2}{\gamma_2} = \frac{\sin\varphi_{12}}{\gamma_{12}} \tag{4.8}$$

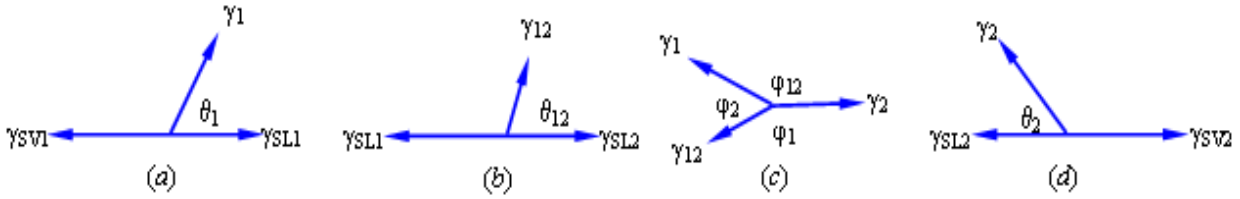

Figure 4.3. Schematic diagrams of three-phase intersection. (*a*) Left droplet/fiber/gas intersection; (*b*) internal droplet/droplet/fiber intersection; (*c*) droplet/droplet/gas intersection at surface; (*d*) right droplet/fiber/gas interaction

There exist two trivial limiting cases of engulfing and non-engulfing, in which the morphology and surface energy of the droplet-on-filament systems can be determined explicitly based on the solution of a monolithic droplet wetting on a filament (Wu and Dzenis, 2006). In the general case of partial engulfing, to avoid the complicate discussions of various connecting conditions in solving Eq. (4.6), we will establish a computational microfluidic droplet model and employ an efficient SFEM to determine the morphology and surface energy of the droplet-on-filament systems and their dependencies upon the model parameters.

4.2.2. Engulfing and Non-engulfing of Two Immiscible Droplets on A Filament

In the case of two immiscible droplets engulfing on a filament, one droplet is completely enwrapped within the second one as illustrated in Figure 4.4.

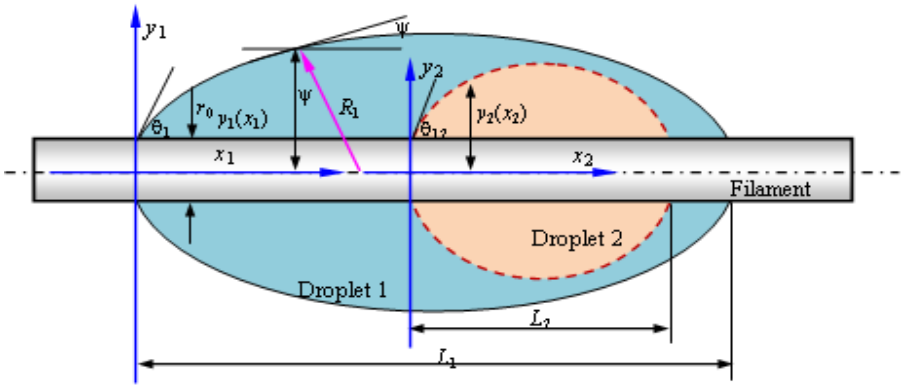

Figure 4.4. Schematic diagram of two immiscible droplets engulfing on a filament

This situation happens when the interfacial energy between two droplets is lower than the surface tension of either droplet since droplet engulfing can reduce the total surface energy of the droplet-on-filament system. In this case, the morphologies of the two droplets can be determined by solving Eq. (4.6) of a monolithic barrel-shaped droplet wetting on a filament (left-half droplet due to the symmetry) (Starov et al., 2007; Wu and Dzenis. 2006):

$$x_i = \int_{y_i}^{y_{i0}} (y_i^2 + \lambda_i r_0 y_{i0}) / \sqrt{(y_{i0}^2 - y_i^2)(y_i^2 - \lambda_i^2 r_0^2)}\, dy_i,\ (i = 1, 2) \tag{4.9}$$

where i = 1 and 2 are corresponding to the first and second droplets, respectively, and

$$\lambda_1 = (y_{10} \cos\theta_1 - r_0) / (y_{10} - r_0 \cos\theta_1) \tag{4.10}$$

$$\lambda_2 = (y_{20} \cos\theta_{12} - r_0) / (y_{20} - r_0 \cos\theta_{12}) \tag{4.11}$$

x_i (i =1,2) are defined with the origin located at the left end of droplets 1 and 2, respectively, y_{i0} (i = 1,2) are the peak radii (at the middle) of droplets 1 and 2 along the vertical symmetric axis, respectively.

Thus, the wetting lengths L_i (i = 1, 2) of droplets 1 and 2 on the filament can be determined by setting $y_i = r_0$ (i = 1, 2) as

$$L_i = \int_{r_0}^{y_{i0}} (y_i^2 + \lambda_i r_0 y_{i0}) / \sqrt{(y_{i0}^2 - y_i^2)(y_i^2 - \lambda_i^2 r_0^2)}\, dy_i.\ (i = 1, 2) \tag{4.12}$$

In the above, y_{i0} (i = 1, 2) can be determined according to the volumes of the two droplets:

$$V_1 + V_2 = \int_{r_0}^{y_{10}} y_1^2 (y_1^2 + \lambda_1 r_0 y_{10}) / \sqrt{(y_{10}^2 - y_1^2)(y_1^2 - \lambda_1^2 r_0^2)}\, dy_1 \tag{4.13}$$

$$V_2 = \int_{r_0}^{y_{20}} y_2^2 (y_2^2 + \lambda_2 r_0 y_{20}) / \sqrt{(y_{20}^2 - y_2^2)(y_2^2 - \lambda_2^2 r_0^2)}\, dy_2 \tag{4.14}$$

Each of the above integral equations can be conveniently solved by means of numerical methods developed in our previous studies (Wu and Dzenis, 2006). Consequently, plugging y_{i0} (i = 1, 2) into Eqs. (4.9) and (12) determines the morphologies and wetting lengths of the two droplets, respectively.

In the case of two droplets wetting but non-engulfing on a filament, the wetting behaviors of the two droplets are independent. The solutions to the morphology, wetting length, and surface energy of each droplet are the same as those for a monolithic droplet wetting on a filament (Wu and Dzenis, 2006).

4.2.3. Partial Engulfing of Two Immiscible Droplets Wetting on A Filament

In this case, it is inconvenient to directly solve Eq. (4.6) at three droplet portions as shown in Fig. 4.2 under three droplet-end BCs and one three-phase interaction condition at the outer droplet surface (See Figure 4.3) due to involvement of multi-valued functions. Thus, a computational partial-engulfing droplet model is established and the efficient SFEM *Surface Evolver* (Brakke, 1992; Brakke, 2000) is employed for directly determining the morphology, surface energy and capillary pressure of two partial-engulfing droplets on a filament. Based on the minimum potential energy of droplet-on-filament system, SFEM is capable of searching for the morphology of equilibrium state of the two partial-engulfing droplets on a filament via minimizing the global surface energy of system such that

$$\Pi = \min\{\sum_{i=1}^{2}[\gamma_i A_{L_iV} + (\gamma_{SL_i} - \gamma_{SV})A_{SL_i}] + \gamma_{12}A_{L_1L_2}\} \tag{4.15}$$

Under given geometrical constraints (*i.e.*, the constant droplet volumes and geometrical constraints of filament surfaces). In the above, γ_{SLi} and γ_{SV} are respectively the interfacial tensions of solid-liquid and solid-vapor, A_{LiV} and A_{SLi} are respectively the liquid-vapor and solid-

liquid interfacial areas, and A_{L1L2} are the interfacial area between two partial-engulfing droplets. In this study, the computational procedure for solving (4.15) is implemented by the public domain SFEM package: *Surface Evolver* (Brakke, 1992; Brakke, 2000). It has been demonstrated that *Surface Evolver* is an efficient, universal simulation tool capable of solving a wealth of wetting problems involving complex surface facets and multiple liquids.

During the numerical simulation based on *Surface Evolver*, the SFEM model of two partial-engulfing droplets on a filament is built up by first defining two super volume elements that represent the two partial engulfing droplets as shown in Figure 4.5(*a*). Two groups of model parameters are defined as requested by *Surface Evolver*, *i.e.*, geometric parameters: volumes (*i.e.*, V_1 and V_2) of two droplets and filament radius (r), wetting parameters: two contact angles (*i.e.*, θ_1 and θ_2) between the droplets and filament, surface tensions (*i.e.*, γ_1 and γ_2) of two droplets, and interfacial tension (γ_{12}) between two droplets. Similar to those adopted by Wu et al. (Wu et al. 2010; Bedarkar, 2010) and others, the global surface energy of the droplet-on-filament system is used as the criterion for searching for the critical droplet morphology at given geometrical and wetting parameters. Since the solving process of *Surface Evolver* is based on numerical iteration with slow convergence rate at the situation of very fine mesh and very large number of nodes. Therefore, special cares have been taken in the course of generating the Input Data file and refining the droplet mesh in order to accelerate the numerical convergence and maintain the numerical stability. The numerical iteration is terminated when the relative numerical error of the global surface energy of the system is below 1%. Figure 4.5 shows the typical snapshots during a numerical process (the filament is not plotted). It can be observed that the wetting morphology of the droplet-on-filament system secures very good stability after only a few iterations and then maintain such stable morphology till the end of the numerical process.

In addition, due to the axisymmetry of the droplet-on-filament system, half- and quarter-droplet models are further built up and simulated to validate the entire-droplet model (See Figure 4.5). Numerical results indicate that these droplet models are capable of predicting highly accurate surface energy and droplet internal pressures. Figure 4.6 compares a few wetting morphologies of the entire-, half-, and quarter-droplet models with the same geometrical and wetting parameters. It can be observed that the wetting morphologies of the droplets based on the three droplet models are the same, which also validate the present droplet models.

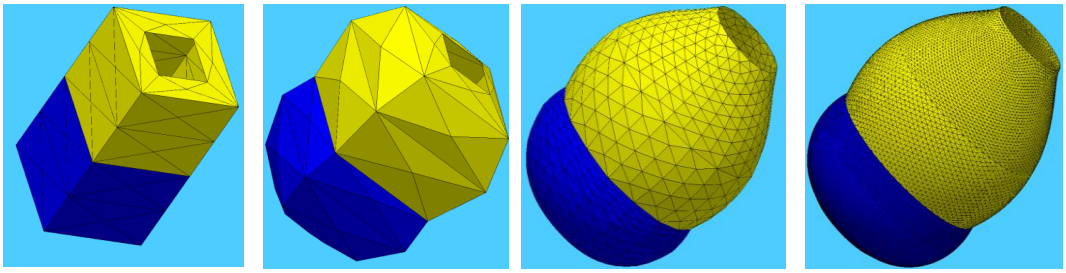

(*a*) (*b*) (*c*) (*d*)

Figure 4.5. Surface finite element analysis of two immiscible droplets partial-wetting on a filament by Surface Evolver. (a): Two super volume elements to represent two immiscible droplets on the filament. (b): Droplet morphology after two numerical iterations. (c): Well stable droplet morphology formed after a few numerical iterations and mesh refinements. (d): Wetting droplet morphology close to the final state after multiple numerical iterations and mesh refinements [The final droplet morphology was obtained using much finer mesh while it is very close to the morphology shown in (d)]. Geometrical parameters: Droplet volumes: V1 = 128 (yellow droplet), V2 = 80 (blue droplet); fiber radius r = 1.5; Wetting parameters: contact angles: $\theta 1 = 35^o$ (yellow); $\theta 2 = 80^o$ (blue); surface tensions: $\gamma 1 = 0.5$ (yellow); $\gamma 2 = 1.0$ (blue); interfacial tension between two droplets: $\gamma 12 = 0.7$

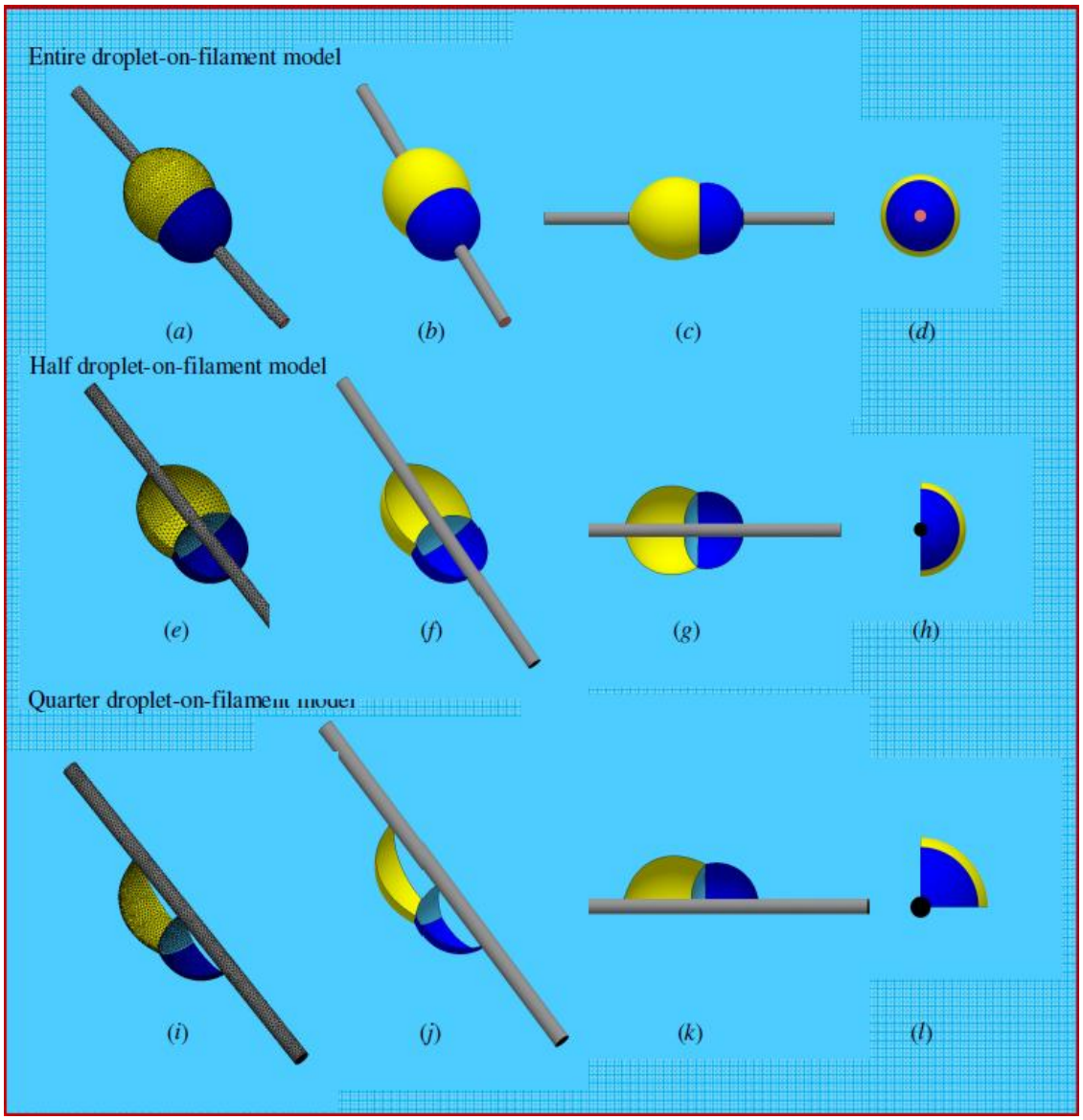

Figure 4.6. Comparison of droplet wetting morphologies based on entire-, half-, and quarter-droplet models of two immiscible droplets partial-engulfing on a fiber by *Surface Evolver*. Column 1: SFEM mesh at the final state; Column 2: 3D view; Column 3: Front view; Column 4: Top view. Geometrical parameters: Droplet volumes: $V_1 = 128$ (yellow droplet), $V_2 = 80$ (blue droplet); fiber radius $r = 1.5$; Wetting parameters: Contact angles: $\theta_1 = 35^o$ (yellow); $\theta_2 = 80^o$ (blue); Surface tensions: $\gamma_1 = 0.5$ (yellow); $\gamma_2 = 1.0$ (blue); Interfacial tension between two droplets: $\gamma_{12} = 0.7$

4.3. Results and Discussions

The above droplet-on-filament models are further exploited for examining dependencies of the surface energy and droplet internal pressure of two partial-engulfing droplets on a filament upon the droplet volume ratio and fiber radius. It needs to be mentioned that all the physical parameters used in the present simulations are dimensionless, which means that when assigning proper units to a few parameters, the units of the rest parameters can be derived properly. For instance, if assigning "N/mm" and "mm" as the units of surface/interfacial tension and fiber radius, respectively, then the unit of surface energy would be "N.mm" and the unit of droplet volume would be "mm^3". Other unit conversions even with scaling can be derived correspondingly. In the following, two groups of numerical simulations are performed for scaling analysis. The selection of specific model parameters does not limit the universal nature of the present droplet models in solving broad wetting problems of droplet-on-filaments. In the first group of simulations, the following model parameters are fixed: geometrical parameter $V_1 = 128$ and fiber radius $r = 0.5$; wetting parameters: contact angles: $\theta_1 = 65^o$ and $\theta_2 = 80^o$; surface tensions: $\gamma_1 = 0.5$ and $\gamma_2 = 1.0$; interfacial tension between two droplets: $\gamma_{12} = 0.7$, while the volume of droplet 2 decreases with the droplet volume ratio V_1/V_2 from 1.0 to 2.0 such that six discrete V_1/V_2 ratios are sampled ($V_1/V_2 = 1.0$, 1.2, 1.4, 1.6, 1.8, and 2.0). At each sampled V_1/V_2 ratio, five simulations are executed to ensure the repetitiveness of the droplet model; half- and quarter-droplet models are also utilized to validate the robustness of the entire-droplet model. Figures 4.7, 4.8 and 4.9 show the variations of the surface energy and droplet internal pressures with respect to the varying droplet volume ratio (V_1/V_2).

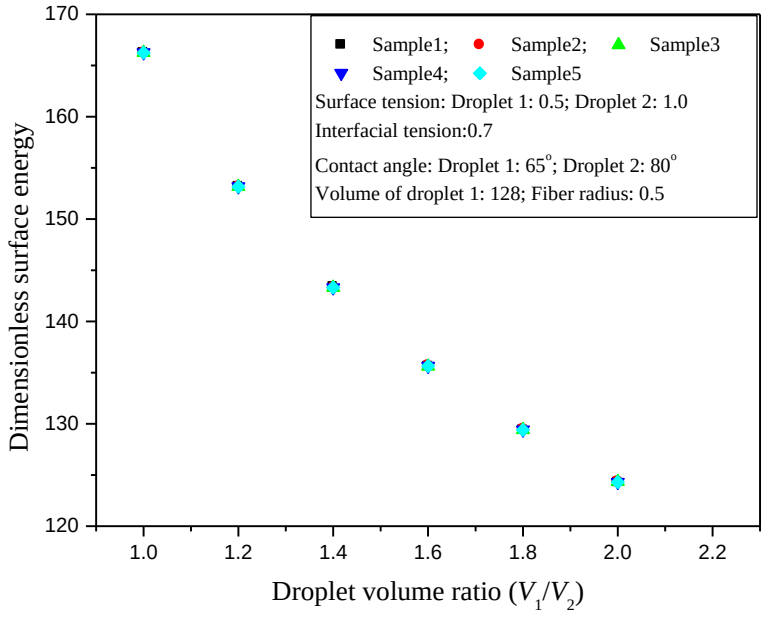

Figure 4.7. Variation of the global surface energy of two partial-engulfing droplets on a fiber with respect to the droplet volume ratio

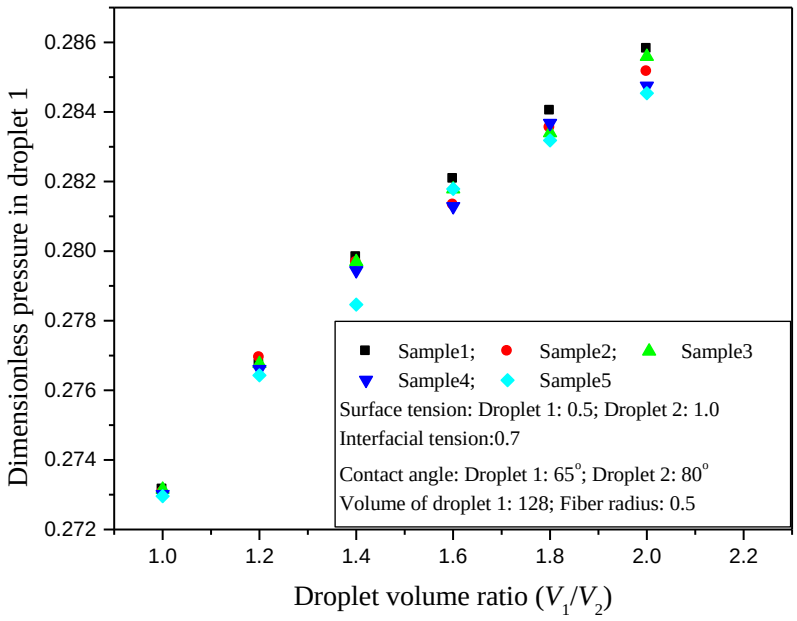

Figure 4.8. Variation of the pressure in droplet 1 of two partial-engulfing droplets on a fiber with respect to the droplet volume ratio

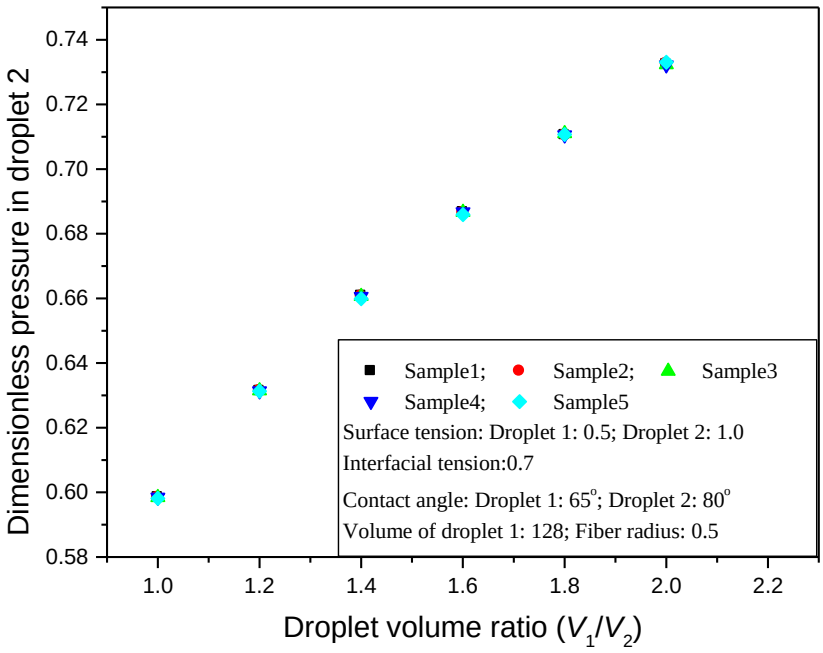

Figure 4.9. Variation of the pressure in droplet 2 of two partial-engulfing droplets on a fiber with respect to the droplet volume ratio

It can be observed from Figs. 4.7 to 4.9 that the numerical experiments show very good numerical convergences, corresponding to the robust droplet model aforementioned and showed in Figures 4.5 and 4.6. Figure 4.7 indicates that at the given model parameters, the global surface energy of two partial-engulfing droplets on a filament decreases nearly linearly with increasing droplet volume ratio. This observation can be understood that given the volume of droplet 1 (V_1), the volume of droplet 2 (V_2) decreases with increasing droplet volume ratio (V_1/V_2), which leads to the decrease of the total volume and surface area of the droplet-on-filament system, i.e., decreasing global surface energy. Figures 4.8 and 4.9 show that the internal pressures in both droplets increases nearly linearly with the increasing droplet volume ratio. Herein, with increasing droplet volume ratio, the volume of droplet 2 (V_2) decreases, corresponding to the decrease of mean principal radius of curvature of droplet 2, *i.e.*, the increase of internal pressure of droplet 2 according to Young-Laplace formula (3). In addition, the increased pressure in

droplet 2 further deforms droplet 1, resulting in the decrease of the mean principal radius of curvature of droplet 1, *i.e.*, the increase of internal pressure of droplet 1 as shown in Figures 4.3-4.8.

In the second group of simulations, the following model parameters are specified: geometrical parameter V_1 = 128; wetting parameters: contact angles: θ_1 = 35^o and θ_2 = 80^o; surface tensions: γ_1 = 0.5 and γ_2 = 1.0; interfacial tension between two droplets: γ_{12} = 0.7. Four droplet volume ratios are used (V_1/V_2 = 1.0, 1.2, 1.4, and 1.6), and the fiber radius r varies from 0.01 to 3.0. Figures 4.10, 4.11, and 4.12 show the variations of the surface energy and droplet internal pressures with respect to the varying fiber radius.

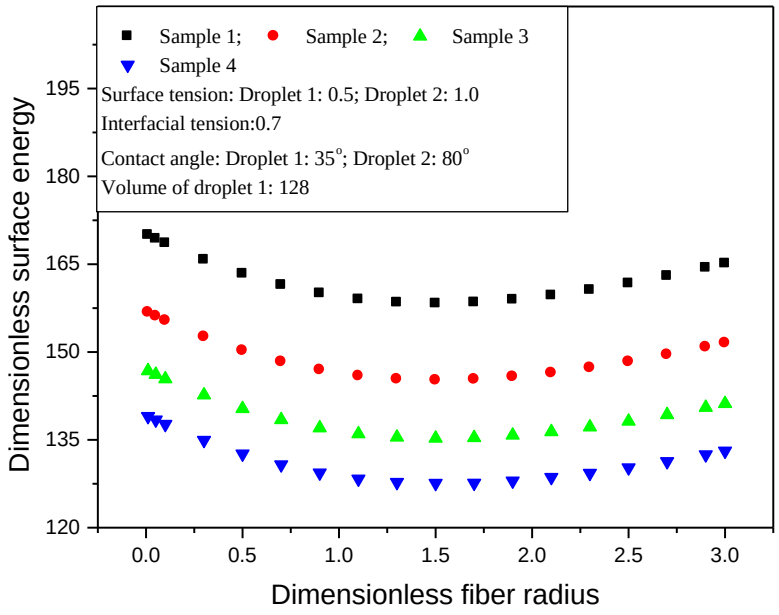

Figure 4.10. Variation of the global surface energy of two partial-engulfing droplets on a filament with respect to the fiber radius

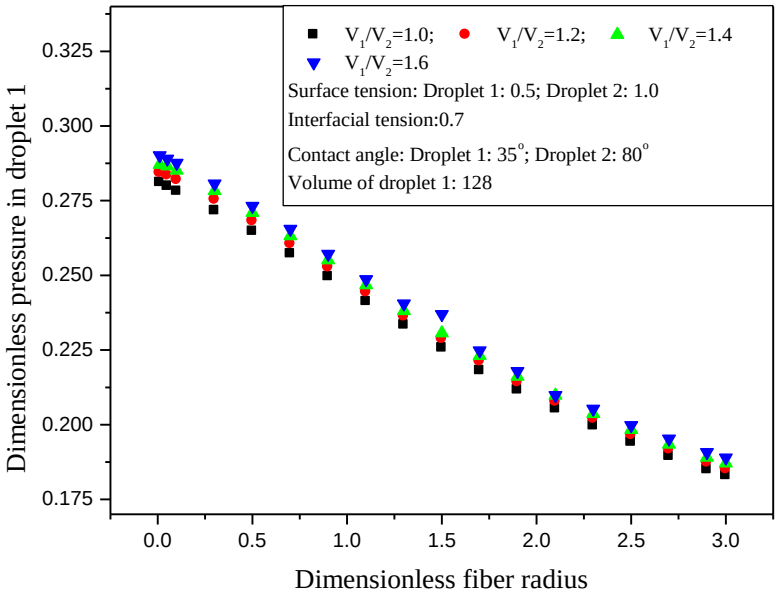

Figure 4.11. Variation of the pressure of droplet 1 of two partial-engulfing droplets on a filament with respect to the fiber radius

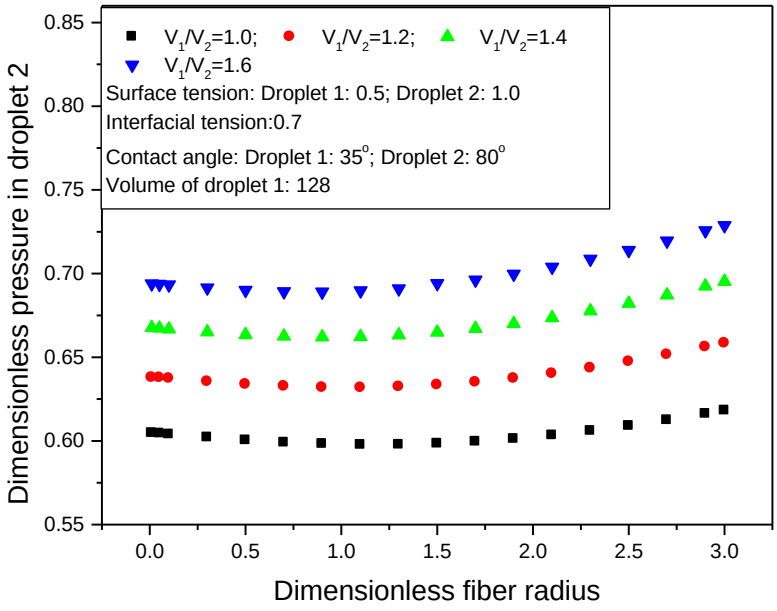

Figure 4.12. Variation of the pressure of droplet 2 of two partial-engulfing droplets on a filament with respect to the fiber radius

Figure 4.10 indicates that given the model parameters, the global surface energy decreases with increasing droplet volume ratio (V_1/V_2) within the range of fiber radius under investigation as expected from the above simulations. In contrast, the global surface energy decreases slightly and then increases with increasing fiber radius for each given droplet volume ratio in this study. The latter indicates that a minimum of global surface energy exists at a critical fiber radius for each droplet volume ratio (V_1/V_2). In addition, Figure 4.11 shows that given a droplet volume ratio (V_1/V_2), the internal pressure of the droplet 1 decreases nearly linearly with increasing fiber radius; while given a fiber radius, it also increases slightly with increasing droplet volume ratio (V_1/V_2) as predicted in the first group of simulations. Figure 4.12 shows that given a droplet volume ratio (V_1/V_2), the internal pressure of droplet 2 decreases slightly and then increases continuously with increasing fiber radius, which also means that a minima of internal capillary pressure of droplet 2 exists at a critical fiber radius. Furthermore, given a fiber radius, the internal pressure of droplet 2 increases with decreasing the droplet volume ratio (V_1/V_2), similar to those predicted in the first group of simulations.

Furthermore, variations of the droplet morphology with respect to the fiber radius at two droplet volume ratios (V_1/V_2 = 1.0 and 1.6) are shown in Figures 4.13 and 4.14. It can be observed that given a fiber radius, the droplet morphology deforms with increasing droplet volume ratio (V_1/V_2). Meanwhile, given a droplet volume ratio (V_1/V_2), the droplet gradually transfers into a thinning torus on the fiber with increasing fiber radius, resulting in a lower principal radius of morphology curvature in the axisymmetric plane, *i.e.*, the higher internal pressure of droplet 2.

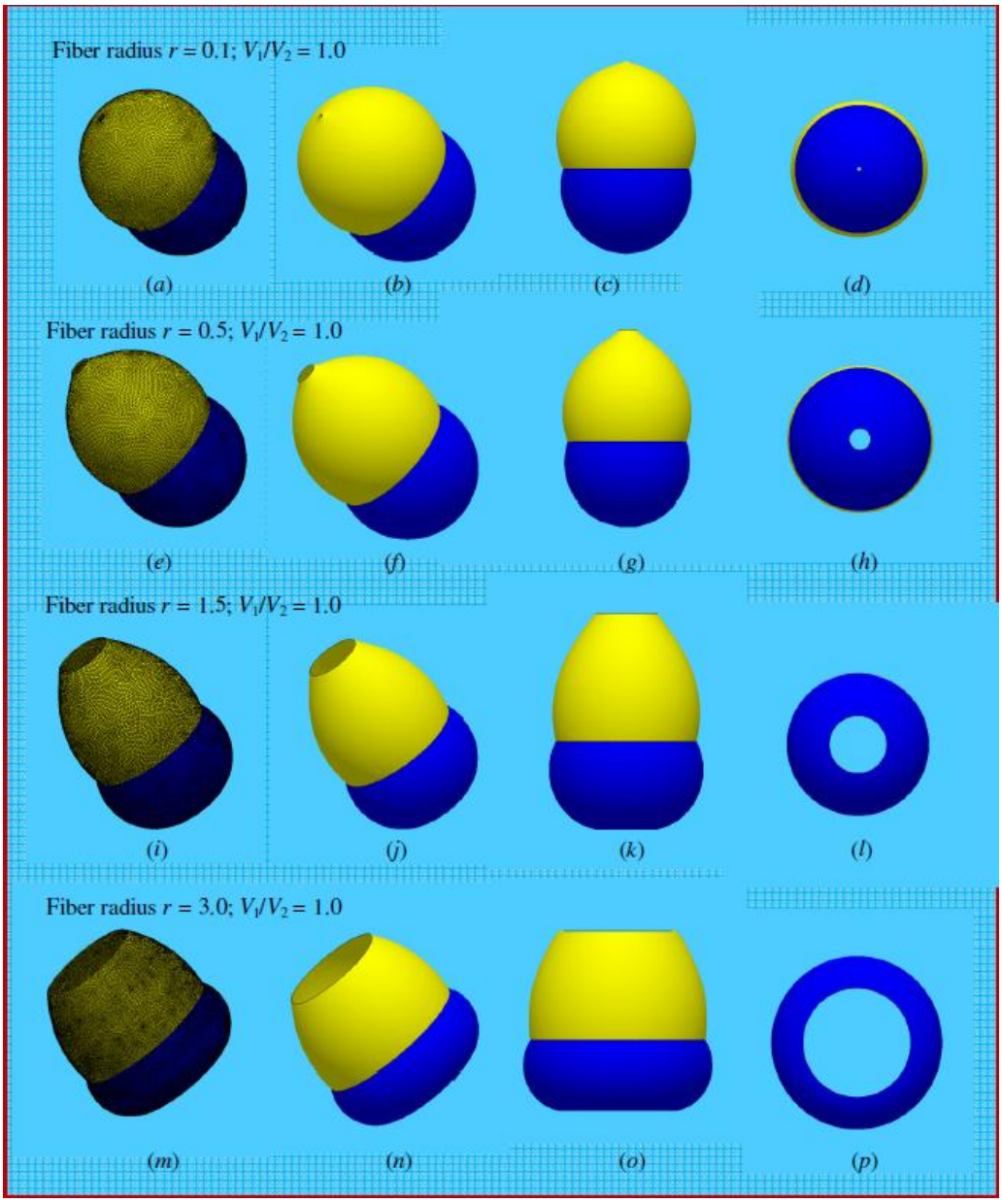

Figure 4.13. Wetting morphologies of two partial-engulfing droplets on a filament with varying fiber radius. Column 1: SFEM mesh at the final state; Column 2: 3D view; Column 3: Front view; Column 4: Top view. Geometrical parameters: Volume of droplet 1 $V_1 = 128$; Wetting parameters: Contact angles: $\theta_1 = 35^o$ and $\theta_2 = 80^o$; surface tensions: $\gamma_1 = 0.5$ and $\gamma_2 = 1.0$; interfacial tension between two droplets: $\gamma_{12}=0.7$

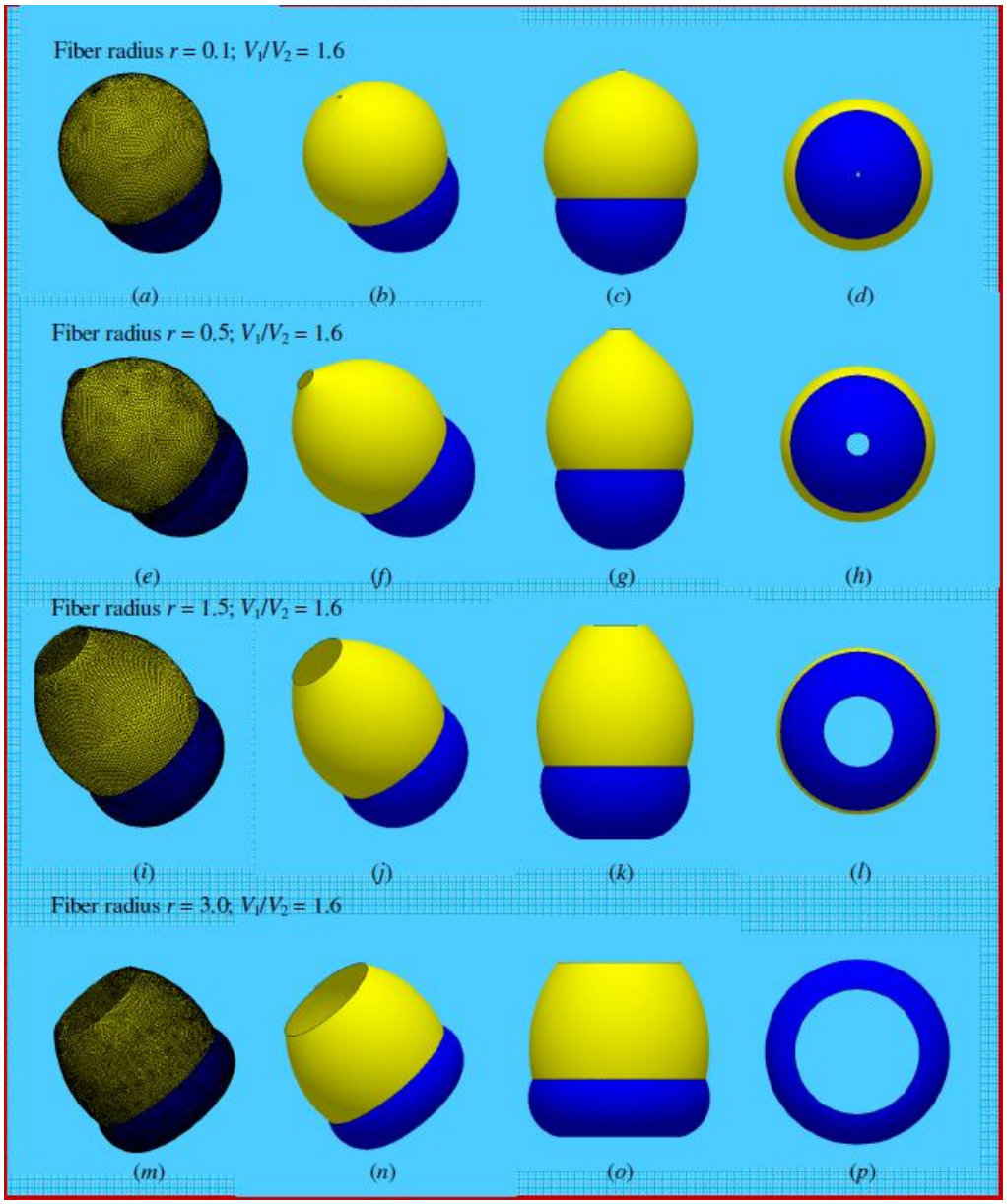

Figure 4.14. Wetting morphologies of two partial-engulfing droplets on a fiber with varying diameters. Column 1: SFEM mesh at the final state; Column 2: 3D view; Column 3: Front view; Column 4: Top view. Geometrical parameters: Volume of droplet 1 $V_1 = 128$; Wetting parameters: Contact angles: $\theta_1 = 35^o$ and $\theta_2 = 80^o$; surface tensions: $\gamma_1 = 0.5$ and $\gamma_2 = 1.0$; interfacial tension between two droplets: $\gamma_{12} = 0.7$

4.4. Summary

The engulfing behavior of two immiscible droplets on a filament has been studied in this chapter. Analytic solutions to two limiting cases of droplet engulfing and non-engulfing have been obtained by extending the previous studies on a barrel-shaped monolithic droplet wetting on a filament. In the case of two immiscible droplets partial-engulfing on a filament, a robust computational droplet model has been established and validated successfully. Detailed numerical simulations have been conducted using the efficient SFEM (*Surface Evolver*) for systematically examining the dependencies of model parameters on the wetting morphology, surface energy, and internal pressure of droplets of the droplet-on-filament systems. It needs to be acknowledged that the present study is still at the beginning of this research area, and quite a few outstanding issues need to be further explored such as the phase diagram of describing the morphology transition among engulfing, non-engulfing, and partial-engulfing of two immiscible droplets on a filament. Yet, due to the involvement of multiple droplets, surfaces and interfaces, explicit solution to such a phase diagram might be extremely difficult to gain; purely numerical simulations based on *Surface Evolver* would also be rather challenging since *Surface Evolver* (based on traditional surface meshing) could not predict the topological transition (phase transition of engulfing) of the droplet-on-filament. Thus, new efficient, suitable numerical methods are still desired for resolving such issue.

In addition, the present computational modeling also provides rich information on two immiscible droplets partial-engulfing on a filament. The numerical scaling analysis has explored the dependencies of wetting morphology, surface energy, and internal pressure of droplets of the droplet-on-filament system upon the wetting properties and geometries of the system. The present study offers a practicable tool that can be utilized for analysis and design of tailorable

wetting properties of textiles and development of novel multifunctional fibrous materials for environmental protection such as oil-spill sorption, oil-water separation, targeted cleaning and liquid sorption, etc.

CHAPTER 5. OIL-WATER SEPARATION

5.1. Introduction

Oil-Water separation is an important technique in human society. It can deal with pollution including polluted water by edible oil in daily life, by collecting the waste edible oil, people can reuse it as fuel. This may reduce the green gas or air pollution by reducing petroleum fuel. Also, in environment protection aspect, Oil-Water separation technique can be employed to collect leaked oil in the ocean (Hosny, 1996); what's more, for the underground oil exploration, this technique can also be used as a method to separate oil-water mixture. Nowadays, oil under the ground is less and less, water is injected underground to make oil go up in order to get the oil from underground. When dealing with the pull-out oil-water mixture, the technique is needed.

5.2. Preliminary Experimental Studies

5.2.1. Preliminary Studies

Exploration of novel, low-cost, high-efficiency oil-spill sorption techniques based on electro-spun nano-fibers have been under intensive investigation in the materials science community and also in the current research group.

To demonstrate the experiment in a clear and understandable way, the commonly used printing paper was used as the control material. Figure 5.1 shows the process of water droplet absorbed by paper. Six snapshots were taken to illustrate the process how water absorption took place in paper material.

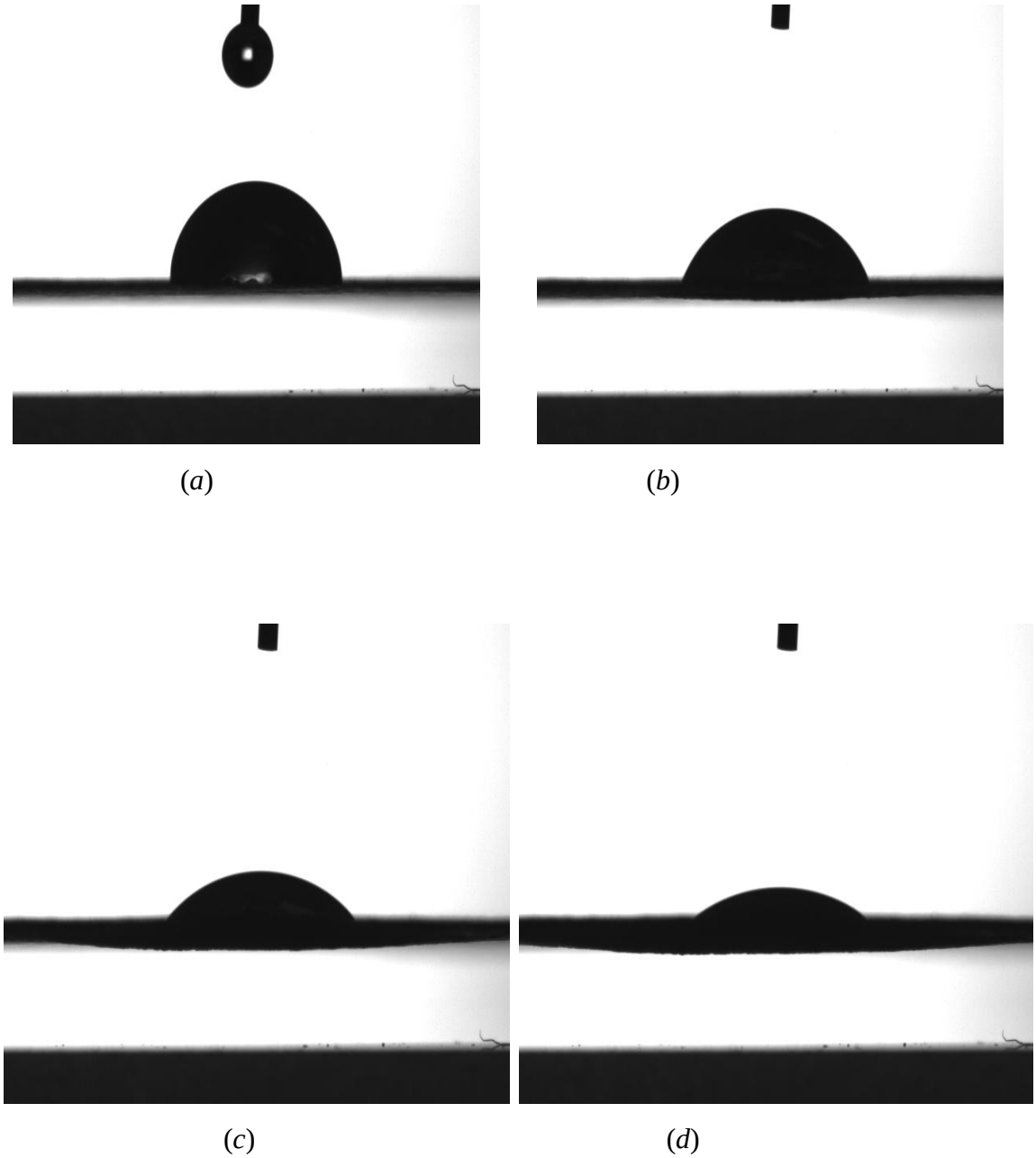

(*a*) (*b*)

(*c*) (*d*)

Figure 5.1. Water-droplet wetting on printing paper. (*a*): The initial time for the droplet contacting with the substrate; (*b*): The state after 15 seconds; (*c*): The state after 30 seconds; (*d*): The droplet shape after 45 seconds; (*e*): The shape after 60 second; (*f*): The state after the water droplet was totally absorbed

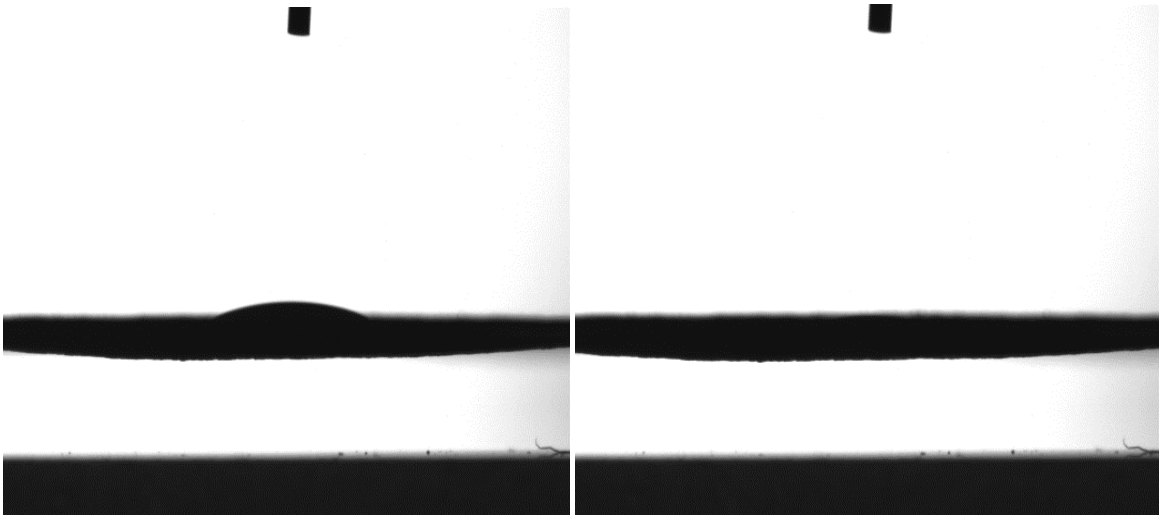

(*e*) (*f*)

Figure 5.1. Water-droplet wetting on printing paper. (*a*): The initial time for the droplet contacting with the substrate; (*b*): The state after 15 seconds; (*c*): The state after 30 seconds; (*d*): The droplet shape after 45 seconds; (*e*): The shape after 60 second; (*f*): The state after the water droplet was totally absorbed (continued)

Figure 5.1 shows a simple process of water sorption with respect to time, which offers the basic concept of how or whether a droplet can exist on a substrate once it is placed on it. Figure 5.2 is the sketch of the FTA1000 Drop Shape Instrument B Frame Analyzer that we used to measure the process of droplets evolution. It can be either applied to tensile droplet contact angle measurement or to the sessile droplet contact angle measurement. Droplet diameter can not be so big in case that the microscope can accurately measure the angle; yet, the substrate should be kept as flat as possible since the contact angle is measured based on horizontal line. Substrates can deform during the sessile test, so, the test should be repeated several time until the angle's variation within 10 degree. An average value is a better way of analysis.

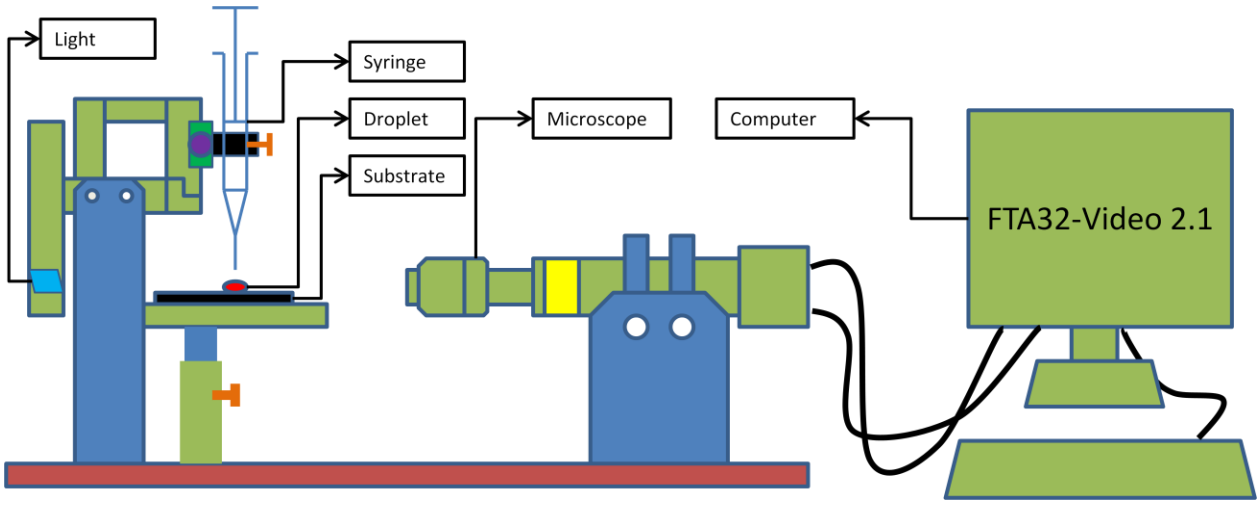

Figure 5.2. Schematic diagram of tool that used to measure contact angle(Drop Shape Instrument B Frame Analyzer System; Model FTA1000; First Ten Angstroms; Courtesy of Dr. Yechun Wang's Research Lab. at the Mechanical Engineering Department at NDSU)

5.2.2. Nanofibrous Materials for Contact Angle Measurement

The nanofibrous materials used in the study of this chapter included graphene-beaded polyacrylonitrile (G/PAN) nanofibers and their carbonized counterpart, and polystyrene (PS) (Mw = 1,000,000 $gmol^{-1}$) nanofibers. Oils included diesel and decane. The mass ratio of graphene in the G/PAN nanofiber was from 0% to 40%. PS nanofibers were produced using PS/tetrahydrofurnan (THF) with the mass concentration of PS from 5% to 20%. These materials were synthesized by Ph.D. student Mr. Zhengping Zhou in Professor Wu's research group at NDSU.

The polymer nanofibers were manufactured by means of electrospinning technique in the laboratory. Figure 5.3 shows two types of electrospinning setups used for nanofiber fabrication in this study, *i.e.*, needle-based electrospinning for laboratory scale nanofiber production and needleless electrospinning for mass production of nanofibers (industrial level).

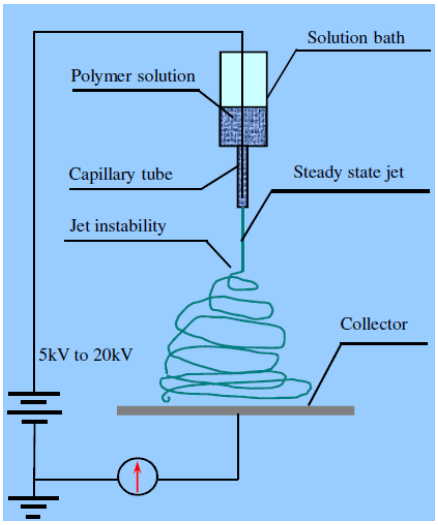

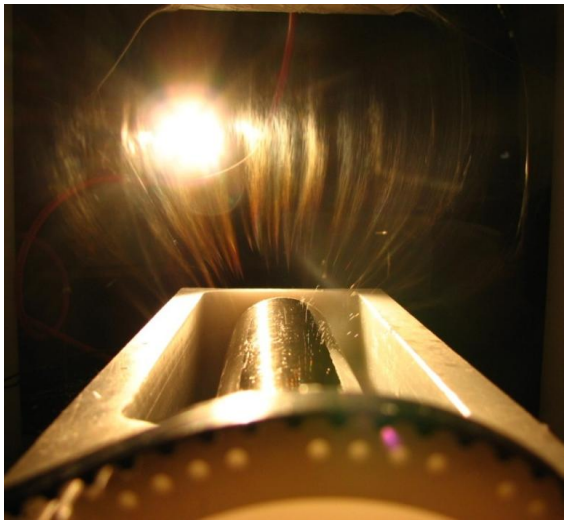

(*a*) (*b*)

Figure 5.3. (a) Schematic diagram of electrospinning setup and (b) Needleless electrospinning machine (Courtesy of Dr. Wu's Research Group at the Mechanical Engineering Department at NDSU)

The process of liquid droplet wetting on carbonized G/PAN nanofibers (40% graphene nanosheets and carbonization under the temperature below 800^{o}C) is shown below. Both water and diesel droplets were tested in order to compare their wetting behavior on nanofiber sheets for the purpose of oil-water separation.

The below four consecutive images were taken with the time duration from 1 second to 100 second after the droplet touched nanofiber films. The wetting experiment showed a stable wetting state.

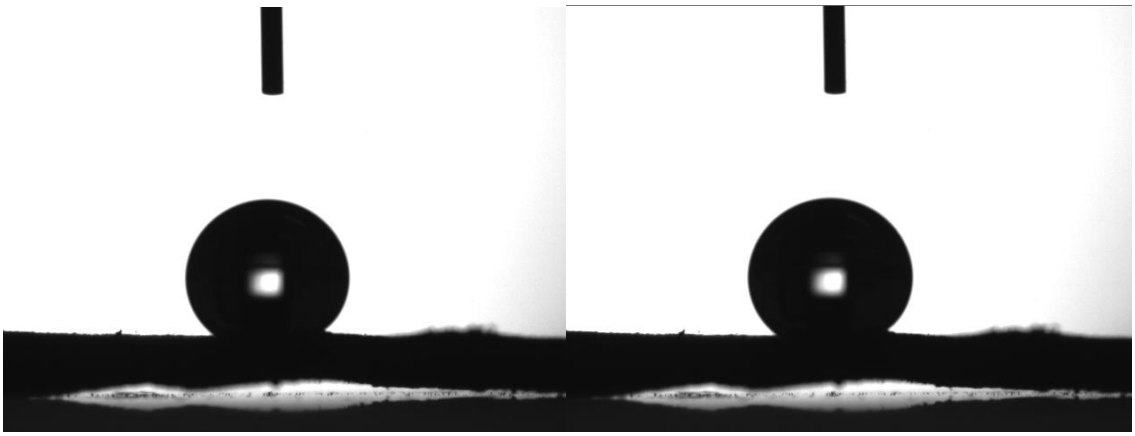

(*a*) (*b*)

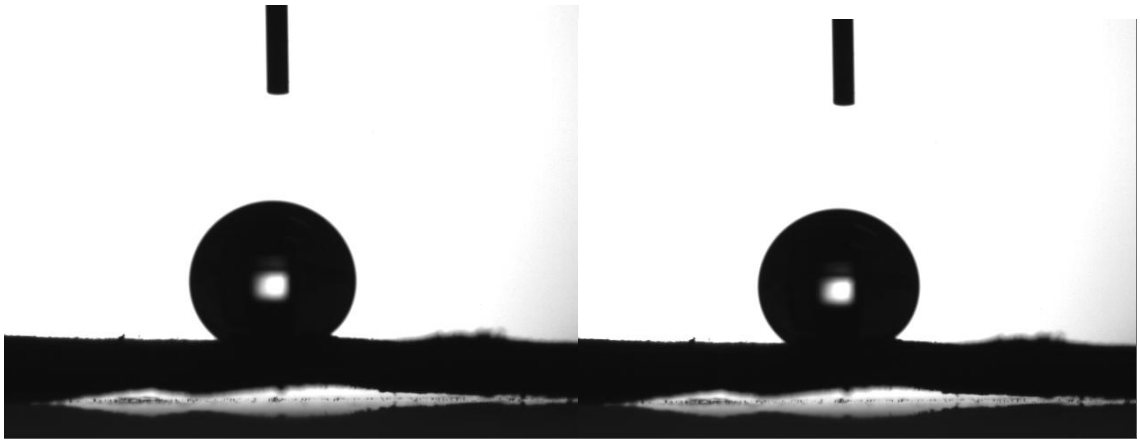

(*c*) (*d*)

Figure 5.4. Snapshots of water droplet wetting on carbonized electrospun G/PAN nanofibers (with 40% graphene nanosheets). (*a*), (*b*), (*c*), and (*d*) are four consecutive snapshots captured in a series instants with the time duration of 100 second. The contact angle here is 137 degree

It can be concluded from the below all images that diesel droplet can completely wet carbonized G/PAN nanofiber fabric (with 40% graphene in mass ratio and carbonization under 800^{o}C.)

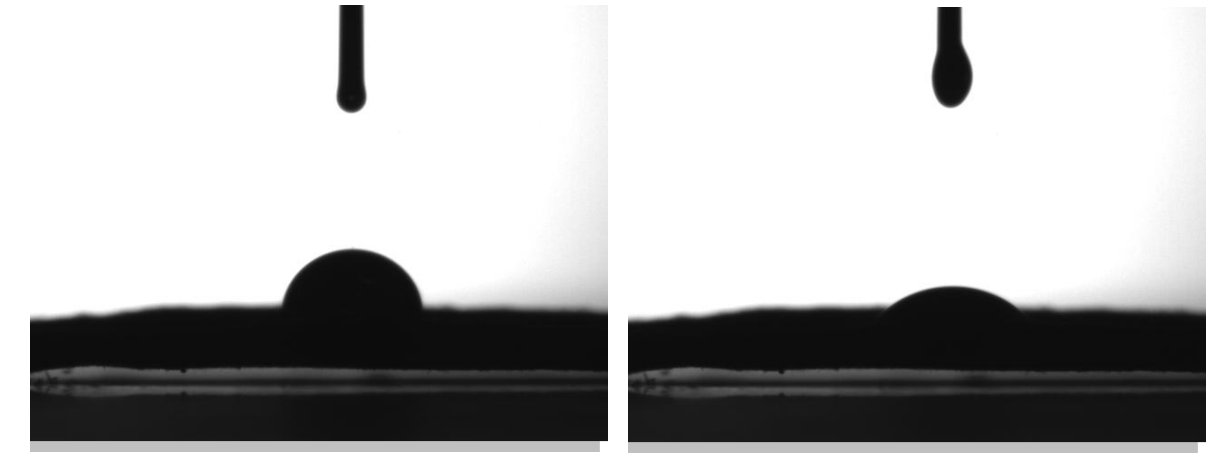

(a) (b)

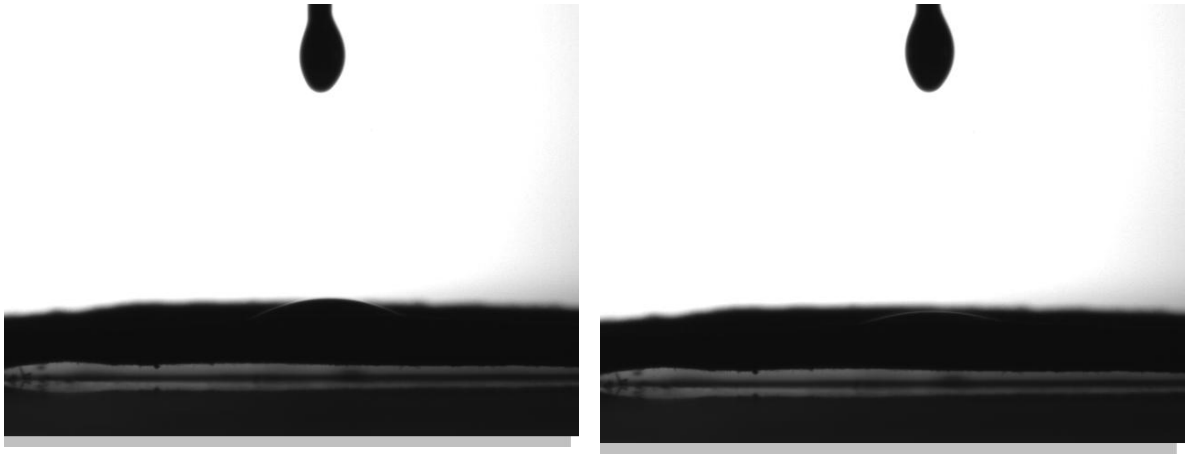

(*c*) (*d*)

Figure 5.5. Snapshots of diesel oil droplet wetting on carbonized G/PAN nanofibers. (*a*), (*b*), (*c*), and (*d*) are the four consecutive snapshots taken in the series instants with the time duration of 6 seconds

5.2.3. PS Nanofibers for Oil/Water Separation

Electrospun PS nanofibers produced using PS/THF solutions were further used for the purpose of oil-water separation. PS is a non-toxic, cheap, easily available material that has wide applications in everyday life, and PS can be reusable. In this experiment, contact angle of water droplet on PS nanofiber fabric was first measured. It has been found that PS nanofibers exhibit varying surface morphology when electrospun using varying PS concentration in PS/THF solution. In this study, five types of PS nanofibers were produced by electrospinning PS/THF solutions with different PS concentration for the purpose of searching for the optimal PS concentration to achieve the maximum water contact angle on the PS nanofiber film. The contact angle of water droplet sitting on the PS nanofiber films was measured, and oil-water separation test was conducted. Images below show the experimental results of oil-water separation test based on the PS nanofibers produced using five different PS concentrations.

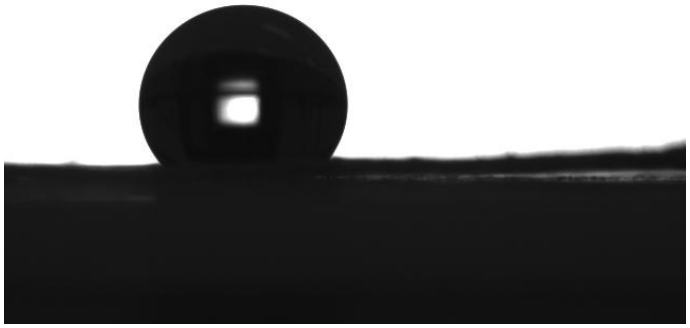

Figure 5.6. Water droplet sits on electrospun PS nanofiber film (5% PS mass concentration of PS/THF). Contact angle: 126 degree

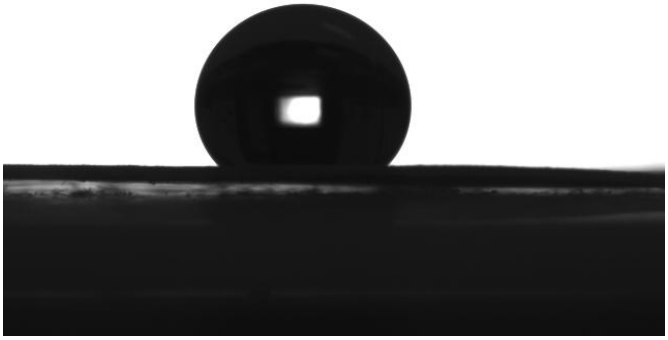

Figure 5.7. Water droplet sits on electrospun PS nanofiber film (8% PS mass concentration of PS/THF). Contact angle: 132 degree

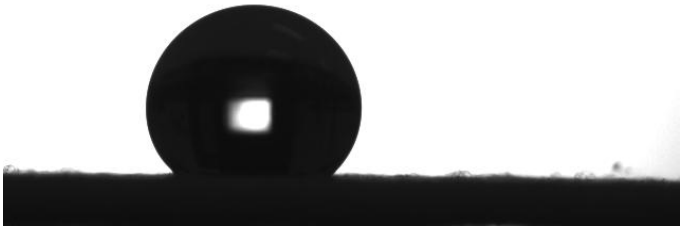

Figure 5.8. Water droplet sits on electrospun PS nanofiber film (10% PS mass concentration of PS/THF). Contact angle: 134 degree

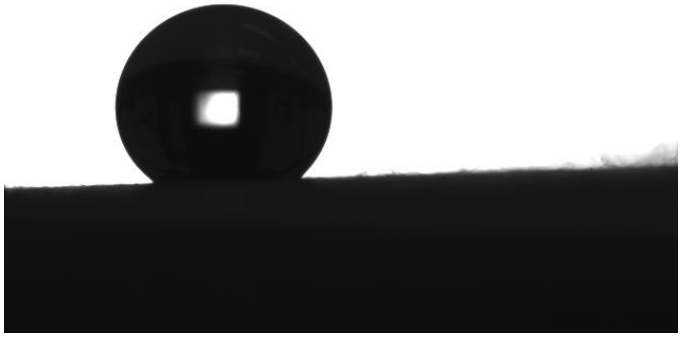

Figure 5.9. Water droplet sits on electrospun PS nanofiber film (15% PS mass concentration of PS/THF). Contact angle: 139 degree

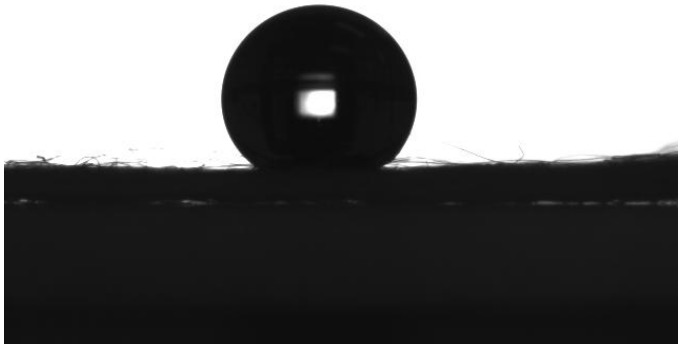

Figure 5.10. Water droplet sits on electrospun PS nanofiber film (20% PS mass concentration of PS/THF). Contact angle: 143 degree

Furthermore, the electrospun PS nanofibers were further utilized for oil-water separation test. Turbidity of the oil-water mixture before and after the separation test was measured using the turbidity testing machine in the laboratory. Oil-Water mixture was prepared by mixing oil and water with volume ratio of 1:1 under the condition of ultrasonic oscillation. Figure 5.11 shows the process of the experiment of oil-water separation. Figure 5.12 shows the oil-water

separation setup and the process of oil/water separation. First, mount the filter on a flask, put material over the filter, pour the mixture of oil and water into it; then the oil flows into the flask through the wall between the material and filter. Water remained on the surface of filter. After the oil is almost in the flask, collect the water to another bottle. The mixture of oil and water which stirred under the sonication machinery was separated into pure water and pure oil.

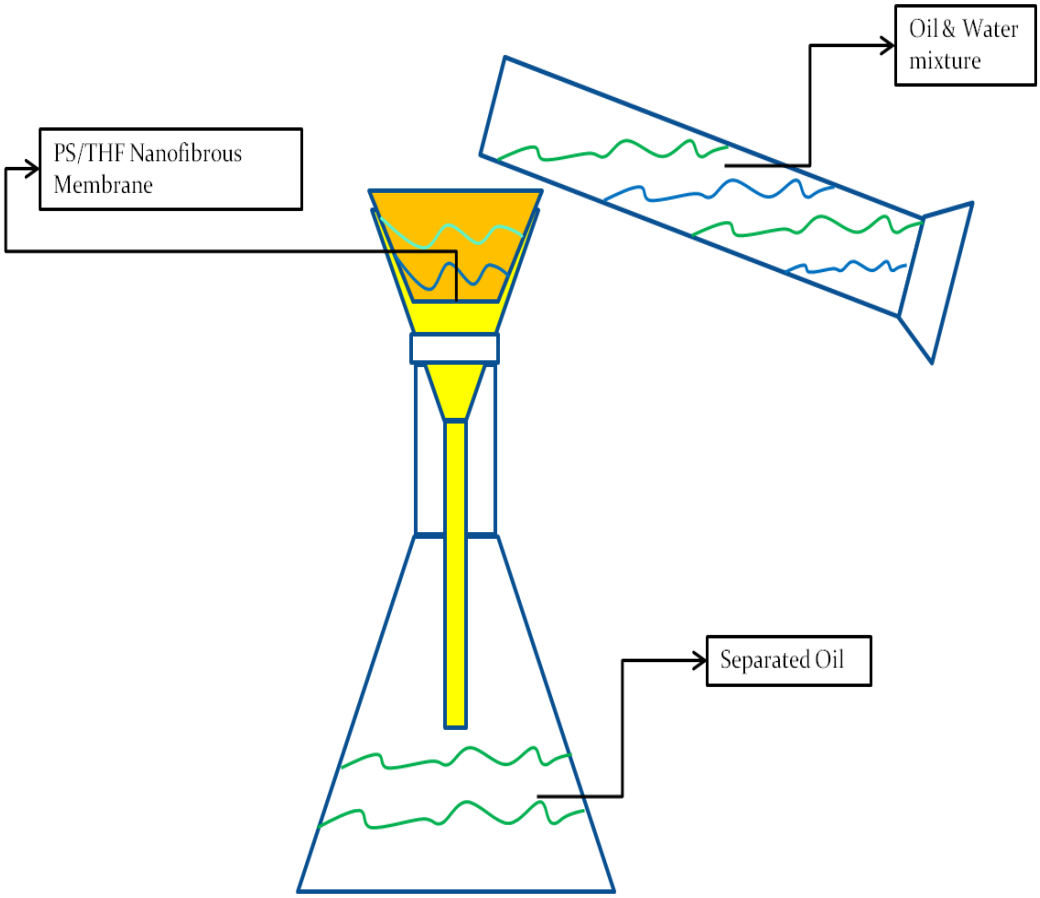

Figure 5.11. Experiment process of oil-water separation(Volume ratio: oil/water: 1:1)

(*a*) (*b*)

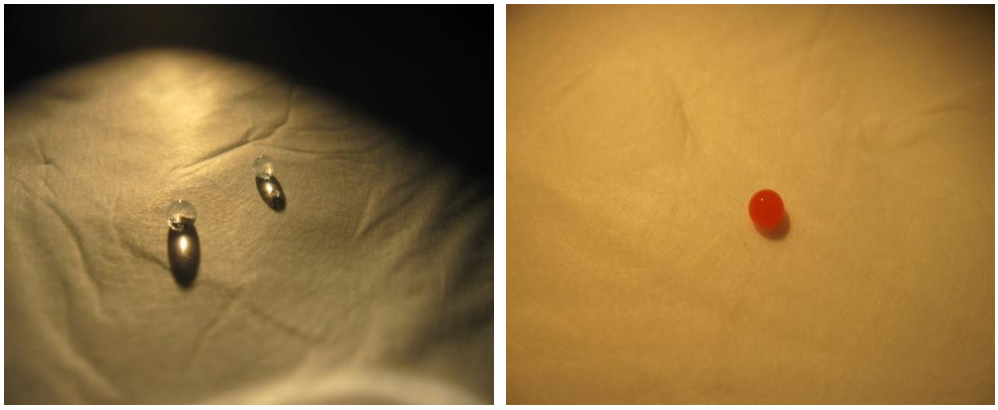

(*c*) (*d*)

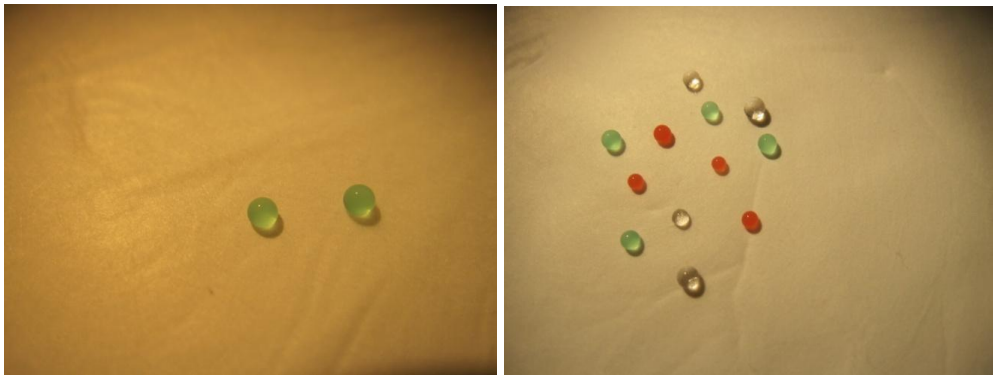

(*e*) (*f*)

Figure 5.12. (*a*) Optical images of oil-water separation with polystyrene (PS) nanofiber membrane; (*b*) filtered oil (left) and water (right); (*c*)-(*f*) water droplets (pure, dyed in red and green) on the mat, showing the superhydrophobicity. (With the aid of Ph.D. candidate Zhengping Zhou in Dr. Wu's research group)

5.3. Results and Discussion

5.3.1. Liquid Wetting Behavior of PAN Based Nano-fibrous Materials

Herein, the experimental results for oil sorption and water resistance were based on G/PAN nanofibers with the graphene mass ration 40%. Figure 5.12 shows the oil/water sorption behavior of the virgin G/PAN nanofibers. For both water and oil, the materials exhibited neither hydrophobic nor oleophobic, which means oil and water can be both absorbed by the G/PAN nanofibers due to the oleophobic properties of graphene nanosheets and the OH groups in PAN. So, so such nanofibrous material is not the targeted material for oil/water separation. After carbonization at the temperature of 800 degree, the carbonized G/PAN nanofibers showed a different wetting performance with the water droplets as shown in Fig. 5.13. From Fig. 5.13(*a*), it can be observed that carbonization does vary the wetting behavior of G/PAN nanofibers to water droplets. However, carbonized G/PAN nanofibers exhibited wetting behavior to oil droplets different from that of the virgin G/PAN nanofibers, *i.e.*, the carbonized G/PAN nanofiber films behaved as oleophilic and hydrophobic. Such nanofibrous material can be potentially used for oil-water separation, and the other nanofibrous materials with hydrophilic and oleophobic wetting behaviors can also be developed for oil-water separation.

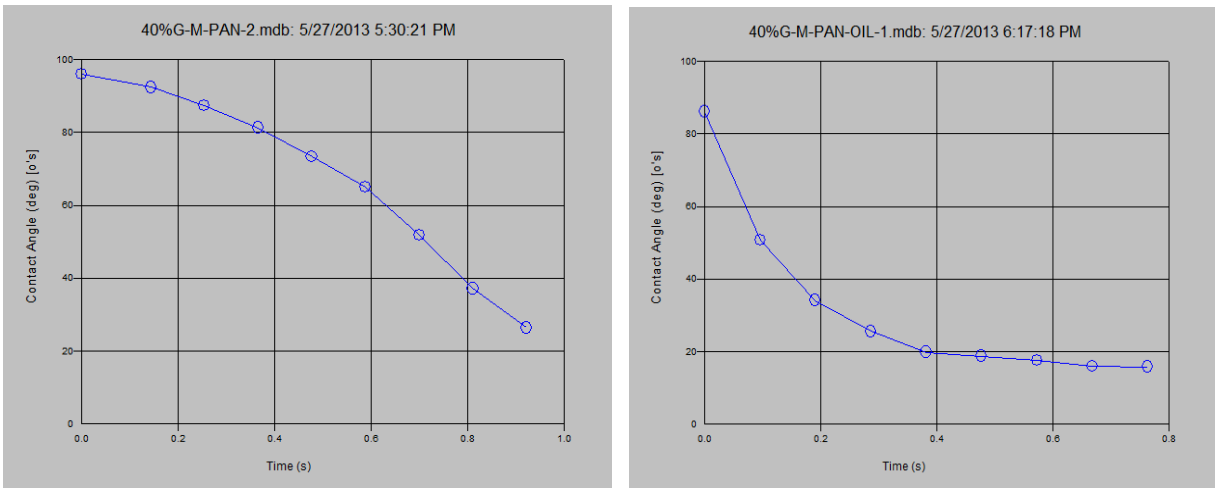

(a) (*b*)

Figure 5.13. Experimental measurements of oil/water sorption on electrospun G/PAN nanofiber film. (*a*) Sorption process of water droplet; (*b*) Sorption process of diesel oil droplet

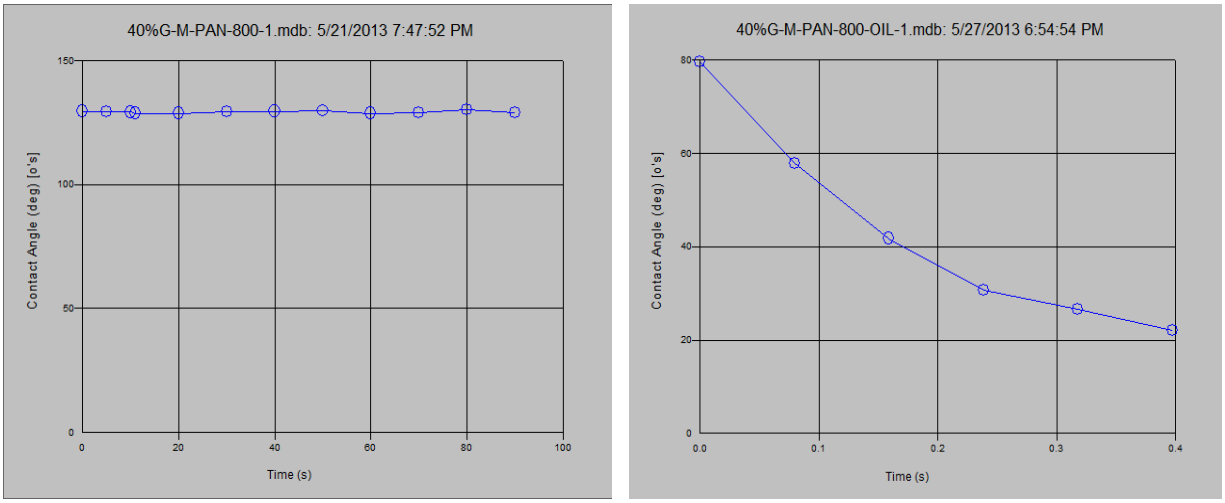

(a) (*b*)

Figure 5.14. Experimental measurements of oil/water sorption on carbonized G/PAN nanofiber film. (*a*): Sorption process of water droplet; (*b*): Sorption process of diesel oil droplet

5.3.2. Experimental Results of PS-Nanofiber Based Oil-Water Separation

Figure 5.14 shows the variation of the contact angles of water droplets on PS nanofiber films produced with varying PS concentration in PS/THF solution. It can be clearly observed that with the increase of PS concentration in PS/THF, the contact angle grows accordingly. At the PS concentration 20%, the contact angle of water droplet is around 144 degrees, very close to superhydrophobic material.

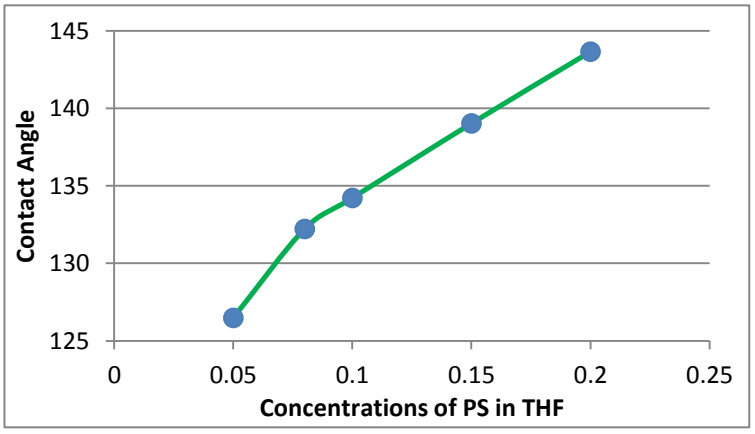

Figure 5.15. Experimental measurements of the contact angle of water droplets on PS nanofiber films electrospun with varying PS concentration in PS/THF solution

Furthermore, electron scanning microscopy (SEM) was employed to characterize the morphology of the PS nanofiber electrospun using varying PS concentration in PS/THF solution. It was observed that the radius of PS nanofibers grows with the increase of PS concentration, which seems to be opposite to the common sense that the smaller feature corresponds to the larger contact angel as prediction by the Cassie-Baxter model. However, the SEM images further indicate that the roughness of nanofiber surface also increases with increasing PS concentration. Thus, the experimental observations can be still explained by the Cassie-Baxter model qualitatively.

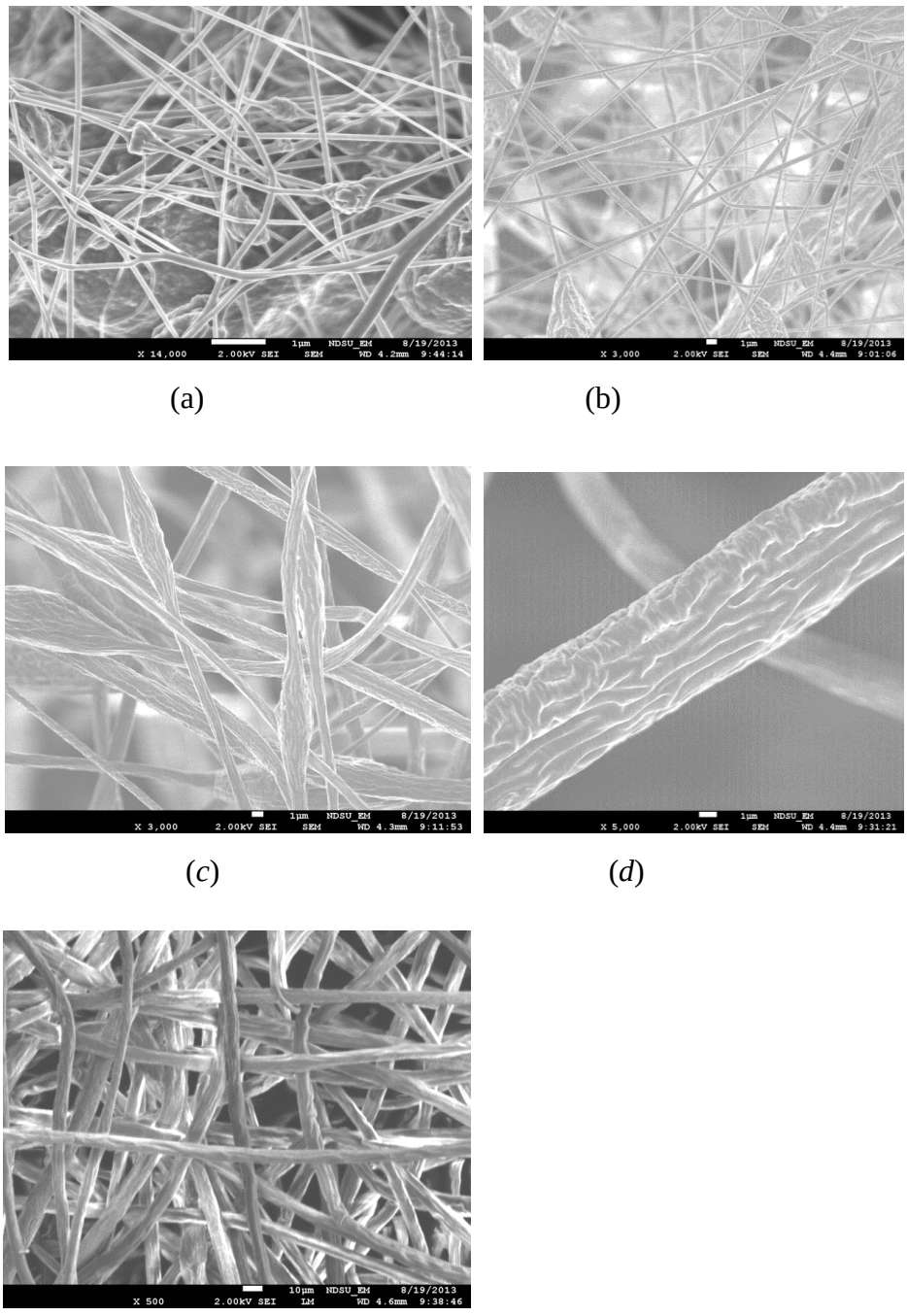

(a) (b)

(*c*) (*d*)

(*e*)

Figure 5.16. SEM images of electrospun polystyrene (PS) nanofibers prepared from (*a*) 5%, (*b*) 8%, (*c*) 10%, (*d*) 15%, and (*e*) 20% by weight concentration in THF

Figure 5.17. Turbidity measured by HACH 2100N Turbidi-meter

Additionally, as a most important criterion for oil-water separation, turbidity separated oil and water are measured. The turbidity of filtrate oil and pure oil are 4.63 and 5.39 NTU, respectively. The turbidity of filtrate and pure water are 0.135 and 48.2 NTU, respectively. The result for water has a big different between filtrate and pure water, it partly because the water can not fall down to the flask and float on the membrane, when water was collected, there is unavoidably some tiny fibers mixed into the water. For turbidity measurement too, tiny dusts can affect the result a lot.

5.4. Summary

In this chapter, experimental studies were performed to investigate the contact angle and wetting behavior of electrospun nanofiber films to oil and water. Experimental results showed that carbonized graphene-beaded PAN nanofibers exhibited very good oleophilic and hydrophobic, which could be utilized for oil-water separation. In addition, PS nanofibers were produced by electrospinning with varying PS concentration in PS/THF. It has been found that the contact angle of water droplet on PS nanofiber films increases with increasing PS concentration

in PS/THF, which was correlated to the increased surface roughness based on SEM studies. First oil-water separation experiment was successfully conducted based on PS nanofiber films. The study indicates electrospun nanofibers could be a promising filtration medium for high-grade oil-water separation.

CHAPTER 6. SUMMARY AND FUTURE WORK

Wetting and spreading of droplets on fibrous materials is ubiquitous in nature, which plays an important role in human life and engineering practice such as fabrication of fabrics with controllable dyeing, cleaning and waterproof behavior. This research is to understand the wetting behavior of droplets wetting on micro/nanofibrous materials and to explore their applications for oil-water separation in environmental protection. Three main tasks have been performed in this thesis research.

(1) Development of new model of capillary force due to liquid bridge. Measurement of capillary force due to a liquid bridge formed between two surfaces is important to study the superhydrophobic and superoleophobic behavior of a variety of new materials under development for oil-water separation and oil-spill sorption. A refined theoretical model of liquid bridge between two flat surfaces is formulated; the related nonlinear ODEs under proper boundary conditions are established and solved analytically and numerically. Scaling analysis of the capillary force under varying liquid volume and surface wetting properties is conducted. The model can be used for data reduction of capillary force measurements and simplification of the experimental process.

(2) Study of the engulfing behavior of two immiscible droplets wetting on a filament. The general governing ODE is established and analyzed in the limiting cases of complete engulfing and non-engulfing. In the partial engulfing case, the morphology and surface energy of the droplet-on-filament system is determined by using a computational SFEM at varying parameters (*e.g.*, contact angle, droplet volume, fiber diameter, etc.) The model can be extended for analysis of the wetting behavior of droplets of oil/water mixture on fabrics, plants, bird feathers, etc. for the purpose of oil-spill sorption.

(3) Development of nanofiber-based oil-water separation technique. Novel continuous polymeric nanofibers with very good hydrophobicity and oleophilicity are fabricated by means of the low-cost electrospinning technique available in the group. A simple process is developed to utilize these nanofibers for oil-water separation. The water quality of the oil-water mixture before and after the oil-water separation is evaluated by means of turbidimetry. The rational mechanism of the process is explored.

This thesis research has reached the preliminary goal of theoretical and experimental study on the wetting behavior of liquid droplets on fibrous materials and its application in oil-water separation. Application of nanofibrous materials for oil-spill sorption and oil-water separation is an emerging research field in environmental science and engineering, which is expected to lead to innovative technologies and technical breakthrough in the near further. Several research topics can be expected along this thesis study as follows.

(1) Synthesis of novel superhydrophobic and superoleophilic nanofibers. The contact angles of water droplet on nanofibers obtained in this study is slight below 150 degrees. The contact angle with 150 degrees is defined as the boundary between superhydrophobic and hydrophobic materials. Thus, new material and new fabrication methods are highly expected for producing new proof-of-concept superhydrophobic and superoleophilic nanofibers for use in oil-spill sorption and oil-water separation.

(2) Elastocapillary study of droplets on micro/nanofibers. At micro and nanoscale, the capillary force due to droplets may dominate the elastic deformation of micro/nanofibers. Thus, a systematic study of elastocapillary phenomena of droplets sitting on micro/nanofibers is highly desired.

(3) Extension and numerical solution of the governing equation of liquid bridge for solving broader microfluidic phenomenon such as liquid bridge between the tip (spherical shape) of atomic force microscope and hard/soft substrate, liquid bridge between fiber filaments, etc.

(4) Numerical simulation of liquid sorption by micro/nanofibrous materials. Novel liquid-fiber interaction models are still desired for efficient, robust modeling the interaction between liquid and multi-fiber or fiber entanglement.

REFERENCES

1. Alava, M.; Dube, M.; Rost, M. "Imbibition in disordered media," Adv. Phys. 53 (2004) 83.

2. Aristoff, J. M.; Duprat, C.; Stone, H. A. "Elastocapillary imbibitions," Int. J. Non-Linear Mech. **46** (2011) 648.

3. Apel, M.; Dew droplet; 2006. http://en.wikipedia.org/wiki/File:Dew_2.jpg.

4. Alvesgaspar; Surface tension: a clip floating in a glass of water, 2009. http://en.wikipedia.org/wiki/File:Surface_tension_March_2009-3.jpg.

5. Bedarkar, A.; Wu, X. F.; Vaynberg, A.. "Wetting of liquid droplets on two parallel filaments," Appl. Surf. Sci. 256 (2010) 7260.

6. Boudaoud, A.; Bico, J.; Roman, B. "Elastocapillary coalescence: Aggregation and fragmentation with a maximum size," Phys. Rev. E 76 (2007) 060102.

7. Butt, H. J.; Graf, K.; Kappl Physics and Chemistry of Interfaces (2nd Edition), Wilet- VCH: Weinheim (2006).

8. Bedarkar, A.; Wu, X. F. "Capillary torque in a liquid bridge between two angled filaments," J. Appl. Phys. 106 (2009) 113527.

9. Bhushan, B.; Jung, Y. C. "Natural and biomimetic artificial surfaces for superhydrophobicity, self-cleaning, low adhesion, and drag reduction," Prog. Mater. Sci. 56 (2011) 1.

10. Booyabazooka, 2008. http://en. wikipedia. org/wiki/File: Wassermolek.

11. Burkersroda, C.V. "Interfacial tension between fluorinerts and silicone oils," In: A. Prakash, J.N.K. (Ed.); J. Phys. Chem. 1993, 5.

12. Bonn, D.; Eggers, J.; Indekeu, J.; Meunier, J.; Rolley, E. "Wetting and spreading," Rev. Modern Phys. 81 (2009) 739.

13. Brochard, F. “Spreading of liquid drops on thin cylinders: the ‘manchon/droplet’ transition,” J. Chem. Phys. 84 (1986) 4664.

14. Bico, J.; Roman, B.; Moulin, L. ; Boudaoud, A. “Elastocapillary coalescence in wet hair,” Nature 432 (2004) 690.

15. Behin, J.; Aghajari, M. “Influence of water level on oil–water separation by residence time distribution curves investigations,” Separation and Purification Tech. 64 (2008) 48-55.

16. Bormashenko, E. (2008). "Why does the Cassie–Baxter equation apply?" Colloids and Surface A: Physicochemical and Engineering Aspects 324: 47–50.

17. Brakke, K.A.; Surface evolver; Exp. Math. 1 141 (1992).

18. Brakke, K.A.; Surface Evolver, 2000, www.susqu.edu/facstaff/b/vrajjer/evolver.

19. Carroll, B. J. “Accurate measurement of contact-angle, phase contact areas, drop volume, and laplace excess pressure in drop-on-fiber systems,” J Colloid Interface Sci. 57 (1976) 488.

20. Carroll, B. J. “Equilibrium conformations of liquid drops on thin cylinders under forces of capillarity,” Langmuir 2 (1986) 248.

21. Chaudhury, M. K. “Direct measurement of interfacial interactions between semispherical lenses and flat sheets of poly (dimethylsiloxane) and their chemical derivatives,” in: Whitesides, G.M. (Ed.); Langmuir 1991.

22. Chou, T. H.; Hong, S. J.; Liang, Y. E.; Tsao, H. K.; Sheng, Y. J. “Equilibrium phase diagram of drop-on-fiber: coexistent states and gravity effect,” Langmuir 27 (2011) 3685.

23. Chen, W. J.; Peng, J. M.; Su, Y. L.; Zheng, L. L.; Wang, L. J.; Jiang, Z. Y. “Separation of oil/water emulsion using Pluronic F127 modified polyethersulfone ultrafiltration membranes,” Separation and Purification Tech. 66 (2009) 591-597.

24. Chen, W. J.; Su, Y. L.; Wang, L. J.; Jiang, Z. Y. “The improved oil/water separation performance of cellulose acetate-graft-polyacrylonitrile membranes,” J. Membrane Sci. 337 (2009) 98-105.

25. Chen, X. M.; Kornev, K. G.; Kamath, Y. K.; Neimark, A. V. “The wicking kinetics of liquid droplets into yarns,” Textile Res. J. 71 (2001) 862.

26. Duprat, C.; Ruyer-Quil, C.; Giorgiutti-Dauphiné, F. “Experimental study of the instability of a film flowing down a vertical fiber,” Eur. Phys. J. Special Topics 166 (1999) 63.

27. Duprat, C.; Aristoff, J. M.; Stone, H. A. “Dynamics of elastocapillary rise,” J. Fluid Mech. 679 (2011) 640.

28. Duprat, C.; Protière, S.; Beebe, A. Y.; Stone, H. A. “Wetting of flexible fibre arrays,” Nature 482 (2012) 510.

29. Dupré, A., 1869; Théorie mécanique de la chaleur, in: Dupré, P. (Ed.). Gauthier-Villars.

30. Du, J. M.; Michielsen, S.; Lee, H. J. “Profiles of Liquid Drops at the Tips of Cylindrical Fibers,” Langmuir 26 (2010) 16000.

31. De Gennes, P. G.; Brochard-Wyart, F.; Quéré, D. “Capillarity and Wetting Phenomena—Drops, Bubbles, Pearls, Waves (translated by A. Reisinger),” Springer, New York, NY (2004).

32. De Gennes, P. G. “Wetting: statics and dynamics,” Rev. Modern Phys. 57 (1985) 827.

33. De Ruiter, R.; de Ruiter, J.; Eral, H. B.; Semprebon, C.; Brinkmann, M.; Mugele, F. “Buoyant droplets on functional fibers,” Langmuir 28 (2012) 1330.

34. Elwenspoek, M.; Tas, N. R. “Elastocapillary fabrication of three-dimensional microstructures,” Appl. Phys. Lett. 97 (2010) 014103.

35. Fan, H.; Gao, Y. X. “Elastic solution for liquid-bridging-induced microscale contact,” J.

Appl. Phys. 90 5904 (2001)

36. Gau, H.; Herminghaus, S.; Lenz, P.; Lipowsky, R. “Liquid Morphologies on Structured Surfaces: From Microchannels to Microchips,” Sci. 283 (1999) 46.

37. Gao, S. Q.; Du, J. Q.; Liu, H. P. “The Liquid-Bridge with Large Gap in Micro Structural Systems,” Scientific Research, J. Modern Phys. pp. 05 (2011) 404-415.

38. Gilet, T.; Terwagne, D.; Vandewalle, N. “Digital microfluidics on a wire,” Appl. Phys. Lett. 95 (2009) 014106.

39. Gilet, T.; Terwagne, D.; Vandewalle, N. “Droplets sliding on fibres,” Eur. Phys. J. E. 31 (2010) 253.

40. Hahn, K., 2009 “ Illustrative diagram of surface tension forces on a needle floating on the surface of water (shown in crossection),” Status: Released to public domain.

41. Hure, J.; Audoly, B. “Capillary buckling of a thin film adhering to a sphere,” J. Mech. Phys. Solids 61 (2013) 450.

42. He, M. Y.; Blum, A. S.; Eric Aston, D.; Buenviaje, C. et al. “Critical phenomena of water bridge in nanoasperity contacts,” J. chem. Phys. 114 1355 (2011)

43. Hudson, J. B. “Surface Science: An Introduction,” John Wiley & Sons, New York (1998).

44. Huang, Z. B.; Liao, X. M.; Kang, Y. Q.; Yin, G. F.; Yao, Y. D. “Equilibrium of drops on inclined fibers,” J. Colloid Interface Sci. 330 (2009) 399.

45. Honsy, A. Y. “Separating oil from oil-water emulsions by electroflotation technique,” Separations Tech. 6 (1996) 9-17

46. Jin, L.; Wojtanowicz, A. K. “Experimental and theoretical study of counter-current oil–water separation in wells with in-situ water injection,” J. Petroleum Sci. and Eng., 2013.

47. Keis, K.; Kornev, K. G.; Neimark, A. V.; Kamath, Y. K. in “Nanoengineered Nanofibrous

Materials," pp. 173, edited by Guceri, S.; Gogotsi, Y.G.; and Kuznetov, V.; Springer (2004).

48. Lorenceau, é.; Quéré, D. "Droplets on a conical fiber," J. Fluid Mech. 510 (2004) 29.

49. Lorenceau, é.; Clanet, C.; Quéré, D. " Capturing drops with a thin fiber," J. Colloid Interface Sci 279 (2004) 192.

50. Li, H. J.; Cao, Y. M.; Qin, J. J.; Jie, X. M.; Wang, T. H.; Liu, J. H.; Yuan, Q. "Development and characterization of anti-fouling cellulose hollow fiber UF membranes for oil-water separation," J. Membrane Sci. 279 (2006) 328-335

51. Liu, J. L.; Feng, X. Q. "On elasto-capillarity: A review," Acta Mech. Sinica 28 (2012) 928

52. Liu, J. L.; Sun, J.; Mei, Y. "Droplet-induced deformation of a polymer microfiber," J. Appl. Phys. 114 044901 (2013).

53. Lmabert, P.; Seigneur, F.; Koelemeijer, S.; Jacot, J. "A case study of surface tension gripping: the watch bearing," J. Micromechanics and Microengineering, No. 7 (2006)

54. Lucas, R. "Rate of capillary ascension of liquids," Kollid Zeitschrift 23 (1918) 15.

55. Syms, R. R. A. "Surface tension powered self-assembly of 3-D micro-opto-mechanical structures," J. Microelectromech Systems 8 (1999) 448.

56. McHale, G.; Newton, M. I.; Carroll, B. J. "The Shape and Stability of Small Liquid Drops on Fibers," Oil Gas Sci. Tech. 56 (2001) 47.

57. McHale, G.; Newton, M. I. "Global geometry and the equilibrium shapes of liquid drops on fibers," Colloids Surfaces A: Physicochem. Eng. Aspects 206 (2002) 79.

58. Starov, M.; Velarde, M. G.; Radke, C. J. "Wetting and Spreading Dynamics," CRC Press, Boca Raton, FL (2007).

59. Neimark, A. V. "Thermodynamic Equilibrium and Stability of Liquid Films and Droplets on Fibres," J. Adhesion Sci. Tech. 13 (1999) 1137.

60. Neukirch, S.; Roman, B.; de Gaudemaris, B.; Bico, J. “Piercing a liquid surface with an elastic rod: Buckling under capillary forces,” J. Mech. Phys. Solids 55 (2007) 1212. [25]

61. Princen, H. M. “Capillary phenomena in assemblies of parallel cylinders: I. Capillary rise between two cylinders,” J. Colloid Interface Sci. 30 (1969) 69.

62. Princen, H. M. “Capillary phenomena in assemblies of parallel cylinders: II. Capillary rise in systems with more than two cylinders,” J. Colloid Interface Sci. 30 (1969) 359.

63. Princen, H. M. “Capillary phenomena in assemblies of parallel cylinders: III. Liquid Columns between Horizontal Parallel Cylinders,” J. Colloid Interface Sci. 34 (1970) 171.

64. Protiere, S.; Duprat, C.; Stone, H. A. “Wetting on two parallel fibers: drop to column transitions,” Soft Matter, 9 (2013) 271.

65. Quéré, D. “Wetting and Roughness,” Ann. Rev. Mater. Res. 38 (2008) 71.

66. Rosen, M. J., 2004. Surfactants and Interfacial Phenomena (3rd ed.). Wiley-Interscience.p., Hoboken, New Jersey.

67. Roman, B.; Bico, J. “Elasto-capillarity: deforming an elastic structure with a liquid droplet,” J. Phys. 22 (2010) C493101.

68. Song, B. H.; Bismarck, A.; Tahhan, R. L; Springer, J. “A Generalized Drop Length–Height Method for Determination of Contact Angle in Drop-on-Fiber Systems,” J. Colloid Interface Sci. 197 (1998) 68.

69. Swain, P. S. and Lipowsky, R. “Wetting between structured surfaces: Liquid bridges and induced forces,” Europhys. Lett. 49 (2), pp. 203-209 (2000)

70. Seemann, R.; Brinkmann, M.; Kramer, E. J.; Lang, F. F.; Lipowsky, R. “Wetting morphologies at microstructured surfaces,” Pro. Natl. Acad. Sci. 102 (2005) 1842.

71. Syms, R. R. A.; Yeatman, E. M.; Bright, V. M.; Whitesides, G. M. “Surface tension powered

self-assembly of microstructures-the state of the art," J. Microelectromech. Systems. 12 (2003) 387.

72. Starov, V. M.; Velarde, M. G.; Radke, C. J. "A Review of: "Wetting and Spreading Dynamics," by V.

73. Virozub, A.; Haimovich, N.; Brandon, S. "Three-Dimensional Simulations of Liquid Bridges between Two Cylinders: Forces, Energies, and Torques," Langmuir 25 (2009) 12837.

74. Van Honschoten, J. W.; Berenschot, J. W.; Ondarcuhu, T.; Sanders, R. G. P.; Sundaram, J. "Elastocapillary fabrication of three-dimensional microstructures," Appl. Phys. Lett. 97, 014103 (2010).

75. Van Honschoten, J. W.; Tas, N. R.; Elwenspoek, M. "Fabrication of three-dimensional microstructures using capillary forces," Transducers Sci. and Tech., 2009.

76. Washburn, E. W. "The dynamics of Capillary Flow," Phys. Rev. 17 (1921) 273.

77. Wagner, H. D. "Spreading of liquid droplets on cylindrical surfaces - accurate determination of contact-angle," J. Appl. Phys. 67 (1990) 1352.

78. Wu, X. F.; Dzenis, Y. A. "Droplet on a fiber: geometrical shape and contact angle," Acta Mech.185 (2006)215.

79. Wu, X. F.; Bedarkar, A.; Vaynberg, K. A. "Droplets wetting on filament rails: Surface energy and morphology transition," J. Colloid Interface Sci. 341 (2010) 326.

80. Wu, X. F.; Bedarkar, A.; Akhatov, I. S. "Hydroelastic analysis of an axially loaded compliant fiber wetted with a droplet," J. Appl. Phys. 108, 083518 (2010).

81. Wu, X. F.; Dzenis, Y. A. "Collapse analysis of nanofibres," Nano-tech. 18 (2007) 285702.

82. Wu, X. F.; Dzenis, Y. A. "Adhesive contact in filaments" J. Phys. D: Appl. Phys. 40 (2007). 4296.

83. Wu, X. F.; Zhou, Z. P.; Zhou, W. M. “Electrical contact resistance in filaments,” Appl. Phys. Lett. 100 (2012) 193115.

84. Wu, X. F.; Dzenis, Y. A. “Elasticity of planar fiber networks,” J. Appl. Phys. 98 (2005) 093501.

85. Wei, Z.; Zhao, Y. P. “Growth of liquid bridge in AFM,” J. Phys. D: 40 (2007) 4368

86. www.foxnews.com/scitech/2010/05/05/chemical-detergents-gulf-oil-disaster/.

87. Xue, C. H.; Ji, P. T.; Zhang, P.; Li, Y. R.; Jia, S. T. “ Fabrication of superhydrophobic and superoleophilic textiles for oil–water separation,” Appl. Surf. Sci. 284 (2013) 464-471.

88. Xue, L. J.; Han, Y. C. “Pattern formation by dewetting of polymer thin film,” Progr. Polym. Sci. 36 (2011) 269.

89. Xue, Z. X.; Cao, Y.Z.; Liu, N.; Feng, L.; Jiang, l. “Special wettable materials for oil/water separation,” J. Mate. Chem. A (2013).

90. Yao, M. W.; McKinley, G. H. “Numerical simulation of extensional deformations of viscoelastic liquid bridges in filament stretching devices,” J. Non-Newtonian Fluid Mech. 74 (1998) 47-88.

APPENDIX

A.1. Surface Evolver Datafiles-Chapter 3

```
// plates_column.fe

 // Evolver data for drop of prescribed volume between two horizontal plates.

 // Contact angle with plates can be varied.

parameter top_angle = 30       // interior angle between plane and surface, degrees

parameter bottom_angle = 30    // interior angle between plane and surface, degrees

parameter height = 0.3          // separation of plates

gravity_constant 0             // start with gravity off

parameter tens = 1

// Contact surface tensions

#define UPPERT  (-tens*cos(top_angle*pi/180))  // virtual tension of facet on plane

#define LOWERT (-tens*cos(bottom_angle*pi/180))

constraint 1    /* the lower plate */

formula: z = 0

energy:         // for contact angle

e1: -(LOWERT*y)

e2: 0

e3: 0

constraint 2    /* the upper plate */

formula: z = height

energy:         // for contact angle and gravitational energy under missing facets

e1: -(UPPERT*y) + G*z^2/2*y
```

e2: 0

e3: 0

content:

c1: z*y

c2: 0

c3: 0

vertices

1 0.0 0.0 0.0 constraint 1 /* 4 vertices on lower plate */

2 1.0 0.0 0.0 constraint 1

3 1.0 1.0 0.0 constraint 1

4 0.0 1.0 0.0 constraint 1

5 0.0 0.0 1.0 constraint 2 /* upper plate */

6 1.0 0.0 1.0 constraint 2

7 1.0 1.0 1.0 constraint 2

8 0.0 1.0 1.0 constraint 2

9 2.0 2.0 -0.25 fixed /* for lower plane */

10 2.0 -1.0 -0.25 fixed

11 -1.0 -1.0 -0.25 fixed

12 -1.0 2.0 -0.25 fixed

13 2.0 2.0 height+0.25 fixed /* for lower plane */

14 2.0 -1.0 height+0.25 fixed

15 -1.0 -1.0 height+0.25 fixed

16 -1.0 2.0 height+0.25 fixed

```
17   2.0  2.0 0.0 fixed   /* for lower plane */

18  2.0 -1.0 0.0 fixed

19 -1.0 -1.0 0.0 fixed

20 -1.0  2.0 0.0 fixed

21  2.0  2.0 height fixed   /* for lower plane */

22  2.0 -1.0 height fixed

23 -1.0 -1.0 height fixed

24 -1.0  2.0 height fixed

edges  /* given by endpoints and attribute */

1   1 2    constraint 1 /* 4 edges on lower plate */

2   2 3    constraint 1

3   3 4    constraint 1

4   4 1    constraint 1

5   5 6    constraint 2 /* upper plate */

6   6 7    constraint 2

7   7 8    constraint 2

8   8 5    constraint 2

9   1 5

10  2 6

11  3 7

12  4 8

13  9 10 no_refine  fixed  /* for lower plate */
```

14 10 11 no_refine fixed

15 11 12 no_refine fixed

16 12 9 no_refine fixed

17 13 14 no_refine fixed /* for upper plate */

18 14 15 no_refine fixed

19 15 16 no_refine fixed

20 16 13 no_refine fixed

21 17 18 no_refine fixed /* for lower plate */

22 18 19 no_refine fixed

23 19 20 no_refine fixed

24 20 17 no_refine fixed

25 21 22 no_refine fixed /* for upper plate */

26 22 23 no_refine fixed

27 23 24 no_refine fixed

28 24 21 no_refine fixed

29 17 9 no_refine fixed   /* for lower plate */

30 18 10 no_refine fixed

31 19 11 no_refine fixed

32 20 12 no_refine fixed

33 13 21 no_refine fixed /* for upper plate */

34 14 22 no_refine fixed

35 15 23 no_refine fixed

36 16 24 no_refine fixed

```
faces  /* given by oriented edge loop */
1   1 10 -5  -9 color lightred
2   2 11 -6 -10 color lightred
3   3 12 -7 -11 color lightred
4   4  9 -8 -12 color lightred
5  13 14 15  16  no_refine density 0 fixed color green /* lower plate for display */
6  17 18 19  20  no_refine density 0 fixed color green  /* upper plate for display */
7  21 22 23 24   no_refine density 0 fixed color green
8  25 26 27 28   no_refine density 0 fixed color green
9  13 -30 -21 29  no_refine density 0 fixed color green
10 14 -31 -22 30  no_refine density 0 fixed color green
11 15 -32 -23 31  no_refine density 0 fixed color green
12 16 -29 -24 32  no_refine density 0 fixed color green
13 25 -34 -17 33  no_refine density 0 fixed color green
14 26 -35 -18 34  no_refine density 0 fixed color green
15 27 -36 -19 35  no_refine density 0 fixed color green
16 28 -33 -20 36  no_refine density 0 fixed color green
bodies  /* one body, defined by its oriented faces */
1   1 2 3 4    volume 1  density 1
read
re := {refine edges where on_constraint 1 }
// Typical evolution
gogo := { re; g 5; r; g 5; r; g 5; hessian; hessian; }
```

A.2. Surface Evolver Datafiles-Chapter 4

```
// 1/1-model of two droplet engulfing on a fiber
parameter rodr = 0.5                    // rod radius
parameter spin = 0.0                    // angular velocity
parameter angle1 = 65                   // internal contact angle with rod
parameter angle2 = 80
parameter tens1 = 0.5                   // surface tension of free surface
parameter tens2 = 1
parameter tens3 = 0.7
// liquid-rod contact energy
#define rode1 (-tens1*cos(angle1*pi/180))
#define rode2 (-tens2*cos(angle2*pi/180))
//initial dimensions
#define ht 2
#define wd 3
// Constraint for vertices and edges confined to rod surface with integral for blob area on
rod
constraint 1
formula: x^2 + y^2 = rodr^2
energy:
e1: -rode1*z*y/rodr
e2: rode1*z*x/rodr
e3: 0
```

```
// Horizontal symmetry plane
constraint 2
formula: z = 0
// Constraint to force vertices on rod to move only vertically.
// Expressed in periodic form, so one constraint fits arbitrarily
// many vertices. Note offset to pi/6 to avoid difficulties with
// modulus discontinuity at 0.
constraint 3 nonnegative
formula: x^2 + y^2 = rodr^2
// Rod surface as one-sided constraint, to keep stuff from caving in
// Can be added to vertices, edges, facets that try to cave in
parameter pp = pi/8    /* to be halved each refinement */
parameter qq = pi/12    /* to be halved each refinement */
constraint 4
formula: (atan2(y,x)+pi/12) % pp = qq
constraint 5
formula: x^2 + y^2 = rodr^2
energy:
e1: rode1*z*y/rodr
e2: -rode1*z*x/rodr
e3: 0
constraint 6
formula: z = -2*ht
```

constraint 7

formula: x^2 + y^2 = rodr^2

energy:

e1: -rode2*z*y/rodr

e2: rode2*z*x/rodr

e3: 0

constraint 8

formula: x^2 + y^2 = rodr^2

energy:

e1: rode2*z*y/rodr

e2: -rode2*z*x/rodr

e3: 0

constraint 9

formula: x^2 + y^2 = rodr^2

energy:

e1: (rode1-rode2)*z*y/rodr

e2: (-rode1+rode2)*z*x/rodr

e3: 0

constraint 10

formula:z=5*ht

constraint 11 // the tube wall, for display

formula: x^2 + y^2 = rodr^2

constraint 12

formula:z=-7*ht

vertices

// equatorial vertices

1 0 -wd 0 constraints 2

2 wd 0 0 constraints 2

3 0 wd 0 constraints 2

4 -wd 0 0 constraint 2

// upper outer corners

5 0 -wd ht

6 wd 0 ht

7 0 wd ht

8 -wd 0 ht

// lower outer corners

9 0 -wd -ht

10 wd 0 -ht

11 0 wd -ht

12 -wd 0 -ht

// vertices on upper rod

13 0 -rodr ht constraints 1,4

14 rodr 0 ht constraints 1,4

15 0 rodr ht constraints 1,4

16 -rodr 0 ht constraints 1,4

// vertices on lower rod

17 0 -rodr -ht constraints 9,4

18 rodr 0 -ht constraints 9,4

19 0 rodr -ht constraints 9,4

20 -rodr 0 -ht constraints 9,4

// second equatorial vertices

21 0 -wd -2*ht constraints 6

22 wd 0 -2*ht constraints 6

23 0 wd -2*ht constraints 6

24 -wd 0 -2*ht constraint 6

// second lower outer corners

25 0 -wd -3*ht

26 wd 0 -3*ht

27 0 wd -3*ht

28 -wd 0 -3*ht

//second rod vertices on lower rod

29 0 -rodr -3*ht constraints 8,4

30 rodr 0 -3*ht constraints 8,4

31 0 rodr -3*ht constraints 8,4

32 -rodr 0 -3*ht constraints 8,4

//on upper rod

33 0 -rodr 5*ht constraint 10,11

34 rodr 0 5*ht constraint 10,11

35 0 rodr 5*ht constraint 10,11

36 -rodr 0 5*ht constraint 10,11

//low rod

37 0 -rodr -7*ht constraint 12,11

38 rodr 0 -7*ht constraint 12,11

39 0 rodr -7*ht constraint 12,11

40 -rodr 0 -7*ht constraint 12,11

edges

// equatorial edges

1 1 2 constraint 2 color black

2 2 3 constraint 2 color black

3 3 4 constraint 2 color black

4 4 1 constraint 2 color black

// upper outer edges

5 5 6

6 6 7

7 7 8

8 8 5

// lower outer edges

9 9 10

10 10 11

11 11 12

12 12 9

// edges on upper rod

13 13 14 constraint 1,4

14 14 15 constraint 1,4

15 15 16 constraint 1,4

16 16 13 constraint 1,4

// edges on lower rod

17 17 18 constraint 9,4

18 18 19 constraint 9,4

19 19 20 constraint 9,4

20 20 17 constraint 9,4

// vertical up outer edges

21 1 5

22 2 6

23 3 7

24 4 8

// vertical low outer edges

25 1 9

26 2 10

27 3 11

28 4 12

// cutting up top face

29 5 13

30 6 14

31 7 15

32 8 16

// cutting up low face

33 9 17

34 10 18

35 11 19

36 12 20

// second equatorial edges

37 21 22 constraint 6

38 22 23 constraint 6

39 23 24 constraint 6

40 24 21 constraint 6

// second lower outer edges

41 25 26

42 26 27

43 27 28

44 28 25

//second edges on lower rod

45 29 30 constraint 8,4

46 30 31 constraint 8,4

47 31 32 constraint 8,4

48 32 29 constraint 8,4

// second vertical up outer edges

49 21 9

50 22 10

51 23 11

52 24 12

// second vertical low outer edges

53 21 25

54 22 26

55 23 27

56 24 28

// second cutting low face

57 25 29

58 26 30

59 27 31

60 28 32

//upperedge

61 33 34 constraint 10,11 fixed

62 34 35 constraint 10,11 fixed

63 35 36 constraint 10,11 fixed

64 36 33 constraint 10,11 fixed

//lower edge

65 37 38 constraint 12,11 fixed

66 38 39 constraint 12,11 fixed

67 39 40 constraint 12,11 fixed

68 40 37 constraint 12,11 fixed

```
//side
69 33 37 constraint 11
70 34 38 constraint 11
71 35 39 constraint 11
72 36 40 constraint 11
faces /* given by oriented edge loop */
// upper side faces
1 1 22 -5 -21 tension tens1 color yellow
2 2 23 -6 -22 tension tens1 color yellow        // Remember you can’t change facet tension
3 3 24 -7 -23 tension tens1 color yellow     // dynamically just by changing tens; you have
4 4 21 -8 -24 tension tens1 color yellow           // to do "tens := 2; set facet tension tens"
5 5 30 -13 -29 tension tens1 color yellow          // top faces
6 6 31 -14 -30 tension tens1 color yellow
7 7 32 -15 -31 tension tens1 color yellow
8 8 29 -16 -32 tension tens1 color yellow
// lower side faces
9  25 9 -26 -1 tension tens1 color yellow
10 26 10 -27 -2 tension tens1 color yellow      // Remember you can change facet tension
11 27 11 -28 -3 tension tens1 color yellow // dynamically just by changing tens; you have
12 28 12 -25 -4  tension tens1 color yellow        // to do "tens := 2; set facet tension tens"
// low faces
13 33 17 -34 -9    tension tens3   color lightblue
14 34 18 -35 -10   tension tens3    color lightblue
```

```
15 35 19 -36 -11   tension tens3   color lightblue
16 36 20 -33 -12    tension tens3  color lightblue
// second upper side faces
17 37 50 -9 -49 tension tens2 color blue
18 38 51 -10 -50 tension tens2 color blue      // Remember you can’t change facet tension
19 39 52 -11 -51 tension tens2 color blue   // dynamically just by changing tens; you have
20 40 49 -12 -52 tension tens2 color blue          // to do "tens := 2; set facet tension tens"
// second lower side faces
21 53 41 -54 -37 tension tens2 color blue
22 54 42 -55 -38 tension tens2 color blue       // Remember you can change facet tension
23 55 43 -56 -39 tension tens2 color blue   // dynamically just by changing tens; you have
24 56 44 -53 -40  tension tens2 color blue         // to do "tens := 2; set facet tension tens"
// second low faces
25 57 45 -58 -41  tension tens2 color blue
26 58 46 -59 -42 tension tens2 color blue
27 59 47 -60 -43 tension tens2 color blue
28 60 48 -57 -44 tension tens2 color blue
29 69 65 -70 -61 constraint 11 color gray
30 70 66 -71 -62 constraint 11 color gray
31 71 67 -72 -63 constraint 11 color gray
32 72 68 -69 -64 constraint 11 color gray
33 61 62 63 64 constraint 10,11 color lightred
34 65 66 67 68 constraint 12,11 color lightred
```

```
bodies /* one body, defined by its oriented faces */

1 1 2 3 4 5 6 7 8 9 10 11 12 13 14 15 16volume 128

2 17 18 19 20 -13 -14 -15 -16 21 22 23 24 25 26 27 28volume 128

3 29 30 31 32 -33 34

read // some initializations

transforms off // just show fundamental region to start with

// special refinement command redefinition

r :::= { autorecalc off; pp := pp/2; qq := qq % pp; 'r'; autorecalc on; }

// a slight perturbation, to check stability

perturb := set vertex y y+.01 where not on_constraint 1

hessian_normal // to make Hessian well-behaved

linear_metric // to normalize eigenvalues
```